

Verena Pfeifer, Travis E. Jones, Juan J. Velasco Vélez, Cyriac Massué, Rosa Arrigo, Detre Teschner, Frank Girgsdies, Michael Scherzer, Mark T. Greiner, Jasmin Allan, Maike Hashagen, Gisela Weinberg, Simone Piccinin, Michael Hävecker, Axel Knop-Gericke, Robert Schlögl

The electronic structure of iridium and its oxides

Journal article | Accepted manuscript (Postprint)

This version is available at <https://doi.org/10.14279/depositonce-5873>



This is the peer reviewed version of the following article:

Pfeifer, V., Jones, T. E., Velasco Vélez, J. J., Massué, C., Arrigo, R., Teschner, D., Scherzer, M., Greiner, M. T., Allan, J. Girgsdies, F., Hashagen, M., Weinberg, G., Piccinin, S., Hävecker, M., Knop-Gericke, A., Schlögl, R. (2015). The electronic structure of iridium and its oxides. *Surface and Interface Analysis*, 48 (5), 261–273. <https://doi.org/10.1002/sia.5895>

which has been published in final form at <https://doi.org/10.1002/sia.5895>. This article may be used for non-commercial purposes in accordance with Wiley Terms and Conditions for Use of Self-Archived Versions.

Terms of Use

Copyright applies. A non-exclusive, non-transferable and limited right to use is granted. This document is intended solely for personal, non-commercial use.

The electronic structure of iridium and its oxides[§]

Verena Pfeifer, Travis E. Jones, Juan J. Velasco Vélez, Cyriac Massué, Rosa Arrigo, Detre Teschner, Frank Girgsdies, Michael Scherzer, Mark T. Greiner, Jasmin Allan, Maike Hashagen, Gisela Weinberg, Simone Piccinin, Michael Hävecker, Axel Knop-Gericke, & Robert Schlögl

Abstract

Iridium-based materials are among the most active and stable electrocatalysts for the oxygen evolution reaction. Amorphous iridium oxide structures are found to be more active than their crystalline counterparts. Herein, we combine synchrotron-based X-ray photoemission and absorption spectroscopies with theoretical calculations to investigate the electronic structure of Ir metal, rutile-type IrO₂, and an amorphous IrO_x. Theory and experiment show that while the Ir 4f line shape of Ir metal is well described by a simple Doniach–Šunjić function, the peculiar line shape of rutile-type IrO₂ requires the addition of a shake-up satellite 1 eV above the main line. In the catalytically more active amorphous IrO_x, we find that additional intensity appears in the Ir 4f spectrum at higher binding energy when compared with rutile-type IrO₂ along with a pre-edge feature in the O K-edge. We identify these additional features as electronic defects in the anionic and cationic frameworks, namely formally O^{I−} and Ir^{III}, which may explain the increased activity of amorphous IrO_x electrocatalysts. We corroborate our findings by *in situ* X-ray diffraction as well as *in situ* X-ray photoemission and absorption spectroscopies.

[§] This is the peer reviewed version of the following article: "Pfeifer, V., Jones, T. E., Velasco Vélez, J. J., Massué, C., Arrigo, R., Teschner, D., Girgsdies, F., Scherzer, M., Greiner, M. T., Allan, J., Hashagen, M., Weinberg, G., Piccinin, S., Hävecker, M., Knop-Gericke, A., and Schlögl, R. 2016 The electronic structure of iridium and its oxides. *Surf. Interface Anal.*, 48, 258–270, doi: 10.1002/sia.5895."

This article may be used for non-commercial purposes in accordance with Wiley Terms and Conditions for Self-Archiving.

This peer reviewed version is available at <http://doi.org/10.14279/depositonce-5873>, page numbers differ.

Introduction

A major challenge facing efforts to transition to a clean and renewable energy supply is finding feasible means of storing excess energy from intermittent resources. Water electrolysis, which converts electrical into chemical energy by the generation of hydrogen and oxygen from water, is a key technology in this field.¹ The hydrogen generated by this method can either be fed into fuel cells or used in the synthesis of chemical feedstocks. However, to date, a sustainable, economic, and stable system for mass production of hydrogen by water electrolysis is lacking. A factor hampering the successful development of such a system is the sluggish oxygen evolution reaction (OER), which requires the transfer of four electrons and four protons. The proton transfer between the electrodes is typically achieved via proton exchange membranes. While this membrane technology is mature, taking advantage of it involves the development of OER electrocatalysts that are both active and stable under the required acidic working conditions. Conducting iridium oxide is the electrocatalyst that represents the best compromise between high activity and stability in acidic environments.^{2,3}

The high activity of iridium oxides for catalyzing the OER, when compared with other materials, has been discussed for decades.^{4,5} Such studies have revealed that upon electrochemical cycling of bulk Ir metal within a specific potential window, a hydrated, amorphous iridium oxide surface layer forms with an accompanying increase in OER activity.^{6,7} The scarcity of iridium has led researchers to refrain from studies on bulk iridium materials and focus on high surface area iridium oxide structures with the aim of optimizing iridium usage.⁸ From these attempts, it was found that amorphous iridium oxide catalysts exhibit higher OER activities than crystalline ones.^{9,10} These findings have prompted studies aimed at identifying and understanding the nature of the active species in iridium oxide catalysts.

Researchers have tried to correlate the electronic structure of iridium oxide with its OER activity by means of X-ray photoemission spectroscopy (XPS) in an effort to identify active surface species.^{6,11–14} Unambiguous speciation, however, has proven elusive because the combined influence of band structure, electron correlation, and spin-orbit coupling on the electronic structure of iridium oxide has not yet been resolved.¹⁵ For example, as a conductor, the core level spectra of rutile-type IrO₂ are expected to be asymmetric, as described by the Doniach–Šunjić (DS) line shape. However, the Ir 4f spectrum of crystalline rutile-type IrO₂ cannot be fit with the conventional DS line profile. The origin of this peculiar line shape has been debated in literature.^{16–18}

In this study, we investigate two reference iridium oxides, one crystalline and one amorphous, and correlate their electrocatalytic activities with their electronic structures. To develop a well-defined reference, we first combine XPS with theoretical calcu-

lations to explain the origin of the unusual line shape of rutile-type IrO_2 . Subsequently, we complement XPS with the near-edge X-ray absorption fine structure (NEXAFS) of the O K-edge and identify additional species present in the catalytically more active amorphous IrO_x powder. Finally, we test the robustness of our proposed models by *in situ* X-ray diffraction (XRD) and *in situ* XPS/NEXAFS investigations.

Experimental

Powder sample characterization methods

Prior to the X-ray photoemission and absorption experiments, two commercially available iridium oxide powders from Sigma-Aldrich (99.9 % trace metals basis) and AlfaAesar (Premion[®], 99.99 %, trace metals basis) were thoroughly characterized.

First, XRD was used to investigate the powders in the as-received state and after calcination at 1073 K for 50 h in 10^5 Pa O_2 . XRD was measured in Bragg–Brentano geometry on a Bruker AXS D8 Advance θ/θ diffractometer using Ni-filtered $\text{Cu K}\alpha$ radiation and a position-sensitive LynxEye silicon strip detector. The powders were filled into the recess of a cup-shaped sample holder, the surface of the powder bed being flush with the sample holder edge (front loading). Second, the as-received powder morphologies were observed, and their atomic compositions were determined in a scanning electron microscope (SEM) Hitachi S-4800 FEG equipped with a Bruker XFlash detector and an energy dispersive X-ray spectroscopy (EDX) system Quantax. The images were taken with an acceleration voltage of 1.5 kV in SE mode, and the atomic compositions were determined via EDX at 25 kV. After degassing the samples for 3 h at 353 K, the surface area of the powders was measured in N_2 at 77 K by the Brunauer–Emmett–Teller (BET) method using an Autosorb 6-MP from Quantachrome.

Thermal analysis of the samples was carried out via thermogravimetry (TG) and differential scanning calorimetry (DSC) using a Netzsch STA449C Jupiter instrument. The samples were heated to 1073 K at a constant heating rate of 10 K min^{-1} in 21 vol.% O_2 in Ar (100 mL min^{-1}) at 10^5 Pa. The resultant gaseous products were analyzed by a Pfeiffer QMS200 OmniStar quadrupole mass spectrometer. The overall iridium oxidation state of the powders was calculated based on a temperature-programmed reduction (TPR). The TPR profile was measured in a home-built plug-flow fixed-bed reactor in 4.92 vol.% H_2 in Ar (80 mL min^{-1}) at a heating rate of 6 K min^{-1} (end temperature 723 K). The H_2 consumption of 9.8 mg rutile-type IrO_2 and 8.3 mg amorphous IrO_x was measured by a thermal conductivity detector. The detector was calibrated by reducing 34.5 mg of CuO (≈ 99 %, trace metals basis) prior to the measurements. In the oxida-

tion state determination, we assume a standard deviation of 2 % based on repeated measurements of the reduction of a defined amount of CuO.¹⁹

Finally, the OER performance of the powders was evaluated. For this, catalyst inks were prepared from ground iridium oxide powder, 60 % water, 39.6 % isopropanol, and 0.4 % Nafion (5 % perfluorinated resin solution, Sigma-Aldrich). Defined ink volumes were deposited on glassy carbon ring disk electrodes (Pine Instruments) with a micropipette and dried in air at 333 K for 30 min to achieve a constant loading of $20 \mu\text{g}_{\text{Ir}} \text{cm}^{-2}$. Electrochemical measurements were performed at a rotational frequency of 1600 rpm in N₂-saturated 0.5 M H₂SO₄. For the linear sweep voltammetry (LSV), the potential was increased at a rate of 5 mV s^{-1} up to 1.8 V versus the standard hydrogen electrode (SHE).

NAP-XPS and NEXAFS

X-ray photoemission and absorption measurements were performed in a near-ambient-pressure X-ray photoemission spectroscopy (NAP-XPS) system at the Innovative station for *in situ* spectroscopy beam line at the synchrotron facility BESSY II/HZB (Berlin, Germany). The setup is described in detail elsewhere.²⁰ Monochromatic light was used to investigate the electronic structure of an Ir (111) single crystal (MaTecK, 99.99 % trace metals basis) and the two iridium oxide powders, which were pressed into pellets of 8 mm diameter (40 mg powder, 3 t pressing weight). The samples were mounted onto a stainless steel backplate on a sapphire sample holder and fixed by a tantalum wire construction (single crystal) or a stainless steel lid with a 3 mm hole (powder pellets). The sample could be heated via the backplate by an infrared laser. The laser power was adjusted with a proportional integral derivative feedback loop controlled by a K-type thermocouple, which was in contact with the sample surface. The experiments were either performed in UHV ($\approx 10^{-6}$ Pa) or in 25 Pa O₂. The gas flow was controlled by Bronkhorst mass flow controllers, and a constant pressure was ensured by a pressure-regulating valve. The exit slit setting of the beam line was 111 μm for all measurements.

In XPS, a pass energy of 10 eV was chosen, which, for the Ir 4f core line, yielded an approximate resolution of 0.2 eV at 130 eV kinetic energy (KE) of the photoelectrons, 0.3 eV at 450 eV KE, and 0.6 eV at 900 eV KE. The associated inelastic mean free paths of the photoelectrons are $\approx 0.4 \text{ nm}$, $\approx 0.7 \text{ nm}$, and 1.1 nm , according to the model of Tanuma *et al.*²¹ The binding energy was calibrated by measuring the corresponding Fermi edge after each core level measurement.

In NEXAFS, the photon energy was varied from 525 eV to 555 eV by a continuous movement of the monochromator. The Auger electron yield at the OK-edge was mea-

sured with the electron spectrometer to partly suppress the contribution of gas-phase O_2^{22} by setting the KE to 385 eV (pass energy 50 eV). The energy resolution was approximately 0.8 eV.

Prior to the room temperature measurements in UHV, the three types of sample were subjected to different pretreatments. The Ir single crystal was cleaned by cycles of Ar^+ -sputtering (2×10^2 Pa, 1.5 kV, 20 mA, 15 min) and subsequent annealing (873 K, 25 Pa O_2 , 30 min) before a final flashing in UHV to 873 K. The powder from Sigma-Aldrich was washed in Milli-Q water to reduce the amount of impurities and then calcined at 1073 K in 10^5 Pa O_2 for 50 h to achieve phase purity. The AlfaAesar IrO_x was measured as received.

Following UHV measurements, the XPS and NEXAFS of the AlfaAesar IrO_x were measured *in situ*. These experiments were performed by heating the sample in 25 Pa O_2 to 523 K at 5 K min^{-1} . Spectra were collected under these conditions. Afterwards, the temperature was increased to 673 K, and spectra were recorded at a constant temperature.

The fitting of all core level spectra was performed after subtraction of a Shirley background with the commercially available CasaXPS software (www.casaxps.com). In all fits, the peak separation and the peak area ratios between the $Ir 4f_{7/2}$ and the $Ir 4f_{5/2}$ components were constrained to 3 eV and 4:3, respectively. Deviations in the peak area ratios of 5 % were allowed to account for the inevitable inaccuracies evoked by background subtraction and peak area determination of asymmetric peaks. Details on the fit functions can be found in Fairley and Carrick.²³ In brief, $DS(\alpha, n)$ is a DS profile with the asymmetry parameter α that is convoluted with a Gaussian whose width is characterized by an integer $0 \leq n \leq 499$. The $SGL(m)$ function blends the DS function with a Gaussian-Lorentzian sum form on the low binding energy side of the peak maximum. The ratio of the sum form is given by the parameter m (0 pure Gaussian and 100 pure Lorentzian). The $SGL(m)$ allows the spectra to be less Lorentzian in nature than the DS function would predict.

***In situ* X-ray diffraction**

In situ XRD data were collected on a STOE θ/θ X-ray diffractometer (Cu $K\alpha_{1+2}$ radiation, secondary graphite monochromator and scintillation counter) equipped with an Anton Paar XRD 900 *in situ* reactor chamber. The gas feed was mixed with Bronkhorst mass flow controllers using 21 vol.% O_2 in helium at a total flow rate of 100 mL min^{-1} . The effluent gas composition was monitored with a Pfeiffer OmniStar quadrupole mass spectrometer. Before the thermal treatment, the sample was characterized at 298 K with slow XRD scans (15° – 75° 2θ with 0.02° steps, 10 s per step counting time).

During the temperature program, faster scans (1 s per step counting time and 70 min per scan) were performed. The sample was heated to 473 K at 20 K min⁻¹ and then isothermal XRD scans were recorded every 50 K between 473 K and 873 K with intermediate heating ramps of 20 K min⁻¹.

Theoretical background and methods

A major challenge with interpretation of XPS data on iridium oxides stems from their peculiar Ir 4f peak shape, which makes speciation ambiguous. As conductors, electron screening will make the X-ray lines in Ir metal and IrO₂ asymmetric. If, for simplicity, we ignore lifetime, phonon, and instrumental broadening and assume constant excitation matrix elements, the asymmetric line shape is given by

$$I(\omega) = \int_{-\infty}^{\infty} dt e^{-i\omega t} \exp \left[\int_0^{\infty} d\epsilon \frac{N_{\text{eh}}}{\epsilon^2} (e^{-i\epsilon t} - 1) \right], \quad (2.1)$$

where ω is the energy, t is the time, N_{eh} is the electron hole pair excitation spectrum, and ϵ is the excitation energy (see reference 24 and references therein). It is well-known that there is no closed-form solution for this line shape. As such, the asymptotic solution is often employed, which can be found by assuming the density of states (DOS) does not vary, resulting in $N_{\text{eh}} = \alpha\epsilon$, where α is a constant. This solution, with the appropriate broadening, gives rise to the DS line shape.²⁵ Formally, it holds only in the neighborhood of the Fermi energy (E_{F}), but in practice, the asymptotic solution is often an excellent approximation over several electron volts above E_{F} , as is the case for Ir metal (see in the succeeding discussions). However, if the DOS is highly structured, N_{eh} may not be linear in ϵ and the DS line shape will be a poor approximation above the threshold energy, as is the case for IrO₂ (see in the succeeding discussions).¹⁶ In principle, it is possible to compute the line shape numerically if N_{eh} is known with high fidelity. However, faithful computation of the electron hole pair excitation spectrum necessitates an extremely accurate DOS,¹⁶ which in turn requires detailed knowledge of the atomic structure. Unfortunately, we lack such information for the amorphous material used in this work. We can instead estimate deviations from the DS line shape using a one-electron picture by recognizing that, within this approximation, the structured DOS introduces additional “shake-up” satellites not predicted by the asymptotic theory. The positions of these satellites can be found using model systems. Thus, a fit model can be developed wherein the DS line shape is augmented with (Gaussian) shake-up satellites centered at their theoretically predicted binding energies. This approach offers a flexible and chemically intuitive means of linking theory and experiment for the speciation of Ir 4f spectra.

To carry out this program, we require the initial and final states in the photoemission process of each material, states in the absence and presence of a core hole, respectively. The shake-up satellites are due to the excitation of an electron (near E_F) in the absence of a core hole into an unoccupied level in the presence of a core hole and are governed by a monopole selection rule, giving $\Delta l=0$ within a central potential approximation.²⁶ As such, we can determine the nature of potential shake-up satellites by examining the occupied l -resolved DOS in the absence of a core hole and the unoccupied l -resolved DOS in the vicinity of a core hole. To compute these DOSs, we projected the wave functions, obtained by way of density functional theory (DFT) with the Perdew, Burke, and Ernzerhof exchange and correlation potential,²⁷ onto orthogonalized atomic wave functions, generating the projected density of states (PDOS) on the ground state and core-ionized iridium atoms.

All DFT calculations were performed with the Quantum ESPRESSO package²⁸ using a kinetic energy cutoff of 50 Ry and a charge density cutoff of 500 Ry. Spin polarization and scalar relativistic corrections were included. Ultrasoft pseudopotentials were taken from the PSLibrary.²⁹ To compute the OK-edge spectra, two gauge-including augmented wave projectors were added to the $l = 1$ channel of the oxygen pseudopotential. A \mathbf{k} -point mesh equivalent to $(8 \times 8 \times 8)$ for the 24-atom IrO_2 cell (Figure 2.1) was used in all calculations along with Marzari–Vanderbilt cold smearing³⁰ with a smearing parameter of 0.005 Ry.

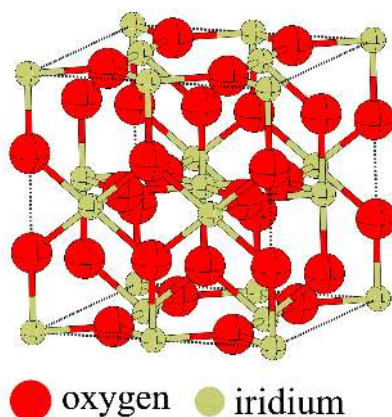


Figure 2.1: Twenty-four-atom supercell of IrO_2 used for calculations.

Before calculating the spectroscopic properties, the rutile-type IrO_2 cell volume was optimized, resulting in $a=b=4.56 \text{ \AA}$ and $c = 3.19 \text{ \AA}$ for the crystallographic unit cell, in good agreement with the $a = b = 4.51 \text{ \AA}$ and $c = 3.16 \text{ \AA}$ measured experimentally.³¹ Ionic relaxations were performed until all components of the forces were less than 103 a. u., while the total change in energy was simultaneously less than 104 a. u.

Spectroscopic properties were computed following the approach detailed in Jones *et al.*³² Briefly, core level binding energies were computed using the Δ SCF (self-consistent field) method to accurately recover initial and final state effects.³³ The relative O 1s binding energies computed with the Δ SCF method were shifted to absolute binding energies using a reference calculation on a (4x4x4) supercell of rutile-type IrO₂, for which we took the measured O 1s binding energy to be 530.0 eV. The relative Ir 4f binding energies were shifted to their absolute values using a reference calculation on a (4x4x4) supercell of Ir metal, which we took to have an Ir 4f_{7/2} binding energy of 60.8 eV. We verified that the relative binding energies in IrO₂ were converged to better than 0.1 eV with our computational setup, including supercell size.

OK-edge spectra were computed from Fermi's golden rule using the XSpectra package.^{34,35} Because powders were used in the experiments, we report the trace of the computed absorption cross section tensors. These computed spectra were convoluted using a Lorentzian with an energy-dependent linewidth, $\Gamma(E) = \Gamma_0 + \Gamma(E)$, to account for lifetime broadening. The natural linewidth of oxygen, 0.14 eV,³⁶ was used for Γ_0 . The energy dependence was assumed to scale linearly, $\Gamma(E) = 0.1 (E - E_F)$. This empirical energy dependence was chosen as it has previously been shown to be an effective approximation in a range of materials.^{32,37} Gaussian broadening was also included with a full width at half maximum (FWHM) of 0.6 eV for calculations on rutile-type IrO₂ and 0.8 eV for the defective IrO_x spectra, where the increased FWHM of the latter is used to account for the reduced order in the amorphous samples. E_F of each computed spectrum was set to the computed O 1s binding energy of the absorbing atom. With this method, the OK-edge spectrum of the crystalline bulk oxide, IrO₂, was well reproduced without a core hole on the absorbing atom. As such, we computed all OK-edge spectra without a core hole on the absorbing atom. For a detailed discussion on the core hole effect in DFT, see, for instance, Mauchamp *et al.*³⁸

Results and discussion

Powder sample characterization

A routine XRD characterization of the as-received iridium oxide powders revealed considerable differences in the XRD patterns (Figure 2.2). The Sigma-Aldrich powder exhibits the expected reflections of the rutile-type IrO₂ structure; hence, we call it rutile-type IrO₂. After calcination, the reflections are sharper and more symmetric due to crystallite growth and possibly a higher degree of stoichiometry. In contrast, as received, the AlfaAesar powder exhibits only minor Ir metal reflections. At the diffraction angles corresponding to rutile-type IrO₂ reflections, the diffractogram of

the AlfaAesar powder shows only slight, broad peaks. Therefore, the oxidic part of this powder is X-ray amorphous, and we call the powder amorphous IrO_x . After calcination, sharp rutile-type IrO_2 reflections evolve also in this powder, while the metallic reflections remain unaltered. Thus, only the formerly amorphous part of the sample crystallizes and is possibly further oxidized during the calcination process while the metal remains unchanged. Quantitative Rietveld analysis of the IrO_2/Ir mixture after calcination yields an estimate of 2.4 wt.% Ir metal in the formerly amorphous IrO_x powder.

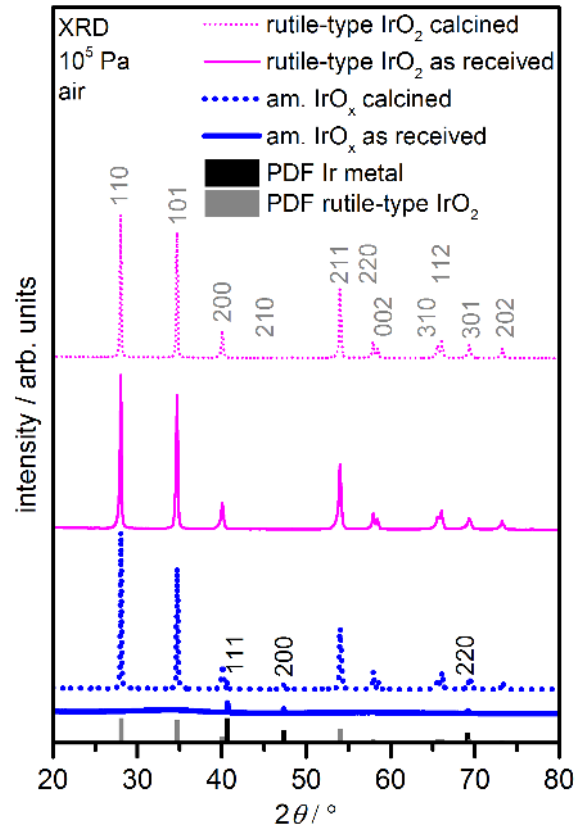


Figure 2.2: X-ray diffraction (XRD) patterns of the IrO_2 and IrO_x powders as received and after calcination at 1073 K in 10^5 Pa O_2 for 50 h. The initially amorphous powder shows as received broad peaks and crystallizes upon calcination. It contains a minor amount of Ir metal. The crystalline powder shows as received all reflections of rutile-type IrO_2 and becomes more homogeneous upon calcination, which is seen by sharper, more symmetric reflections.

The different morphologies of the as-received samples are shown in the scanning electron microscopy images in Figure 2.3. The rutile-type IrO_2 consists of parallelepiped-shaped particles of various sizes, while the amorphous IrO_x is less ordered and is composed of smaller, fluffy particles. EDX reveals the expected 1:2 atomic ratio of Ir:O in the rutile-type IrO_2 , while an oxygen excess is observed for the amorphous IrO_x . In both samples, iron contamination of $\approx 1\%$ was found. The correspond-

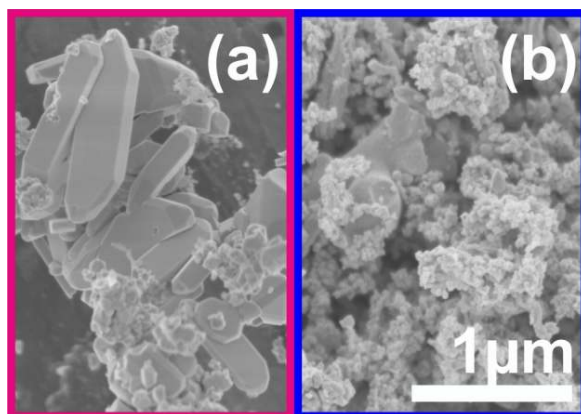


Figure 2.3: Scanning electron microscopy images of (a) the rutile-type IrO_2 powder and (b) the amorphous IrO_x powder. The scale bar applies to both (a) and (b).

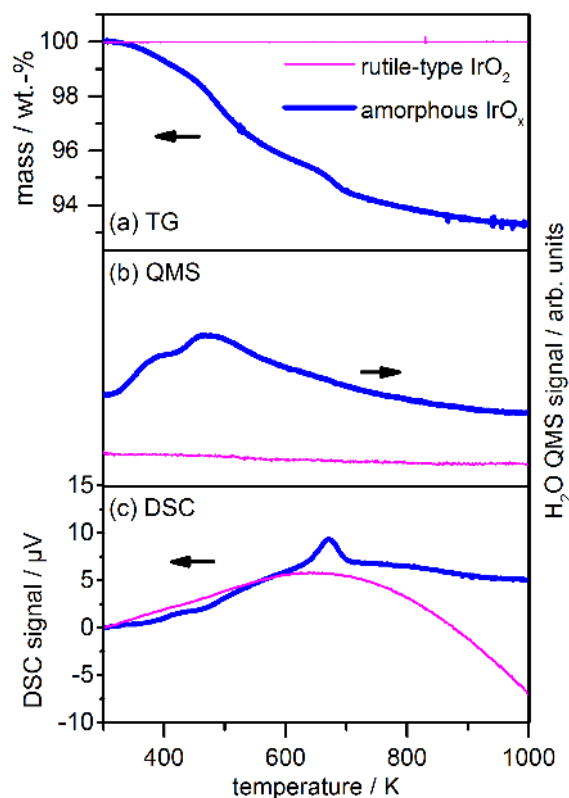


Figure 2.4: Thermogravimetry quadrupole mass spectrometry differential scanning calorimetry (TG-QMS-DSC). (a) The TG signal of the rutile-type IrO_2 is constant over the entire temperature range, while the amorphous powder reduces its mass by 6 wt.%. (b) Corresponding water ($m=18$ a. u.) QMS trace reveals that the weight loss of the amorphous powder is due to physisorbed and chemisorbed water loss. (c) DSC shows by an exothermic peak at 673 K that the amorphous powder crystallizes at this temperature.

ing BET surface area of the crystalline powder is considerably smaller ($2.1 \text{ m}^2 \text{ g}^{-1}$) than that of the amorphous IrO_x ($33.3 \text{ m}^2 \text{ g}^{-1}$).

The TG profile and the corresponding mass spectrum and DSC are shown in Figure 2.4. The rutile-type IrO_2 powder does not show an obvious mass loss upon heating, and only a small amount of CO_2 is released (not shown). In contrast, the amorphous IrO_x loses 6 wt.% upon heating. The H_2O quadrupole mass spectrometry trace shows that at around 400 K ≈ 2 wt.% physisorbed water is released from IrO_x . From ≈ 500 K on, ≈ 4 wt.% chemisorbed water is released from the IrO_x sample. The large amount of water contained in the amorphous IrO_x can account for the deviation from the nominal stoichiometry observed in EDX. An exothermic peak in DSC reveals that the IrO_x sample crystallizes at 673 K. The TPR profiles of both powders are shown in Figure 2.5. The two powders display differences in both their reduction profile and temperature. The rutile-type IrO_2 is reduced at around 500 K in a temperature window of ≈ 75 K, while the amorphous IrO_x is already reduced at 350 K in a temperature window of only ≈ 15 K. Furthermore, the inset of Figure 2.5 reveals that the amorphous powder already adsorbs hydrogen during initial H_2 exposure at room temperature, which needs to be taken into account when determining the overall H_2 consumption of the amorphous IrO_x . Based on the total H_2 consumption, the overall oxidation state of iridium in the two powders is calculated. For the rutile-type IrO_2 powder, an Ir oxidation state of 4.1 ± 0.1 is obtained. This finding is in line with the EDX measurement and the expected formal Ir oxidation state of IV in stoichiometric IrO_2 . To account for only the oxygen-containing iridium species of the amorphous IrO_x , the metallic Ir and physisorbed water contents were subtracted prior to the oxidation state determination of the amorphous IrO_x . In contrast to rutile-type IrO_2 , an Ir oxidation state of 3.6 ± 0.1 is found for the oxygen-containing iridium species in the amorphous powder. Hence, the amorphous powder likely contains iridium-oxygen species with iridium in a formal oxidation state of less than IV, e.g. Ir^{III} , in addition to Ir^{IV} species. We note that this presence of multiple iridium oxidation states has been argued to be crucial for enhanced OER activity.^{39,40}

Indeed, OER activity assessment demonstrates that the amorphous sample is considerably more active than the rutile-type powder (Figure 2.6). The linear sweep voltammetry displays that the onset of the OER is at a lower potential, and the current density shows a steeper increase for amorphous IrO_x . And although the BET surface area of the amorphous powder is larger than that of the crystalline one (16x), it cannot explain the increased activity. It is then likely that the amorphous IrO_x possesses a surface termination that has an intrinsically higher OER activity than that of the surface species of rutile-type IrO_2 .⁹

Our preliminary characterizations have revealed a variety of differences between these commercially available iridium oxide powders: crystalline versus amorphous, no water loss versus 6 wt.% water loss in TG, oxidation state 4.1 versus 3.6 from TPR

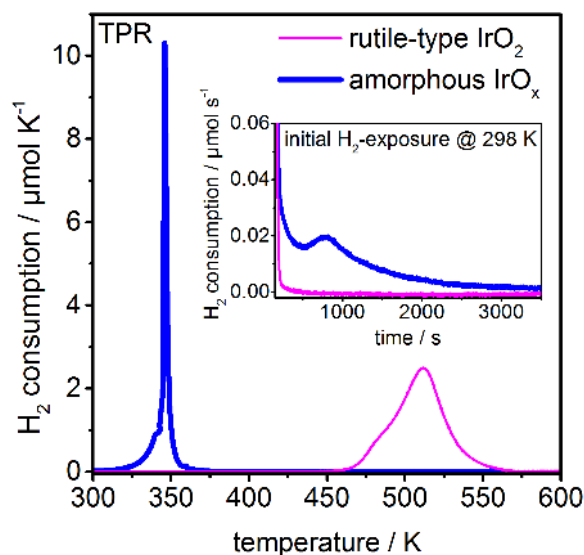


Figure 2.5: Temperature-programmed reduction (TPR) of amorphous IrO_x and rutile-type IrO_2 . The amorphous IrO_x already strongly adsorbs H_2 at room temperature (inset) without releasing water (monitored by quadrupole mass spectrometry; not shown). Upon heating, the amorphous powder is reduced in a narrow temperature window at around 350 K, while the rutile-type IrO_2 is reduced in a broader temperature window at around 500 K.

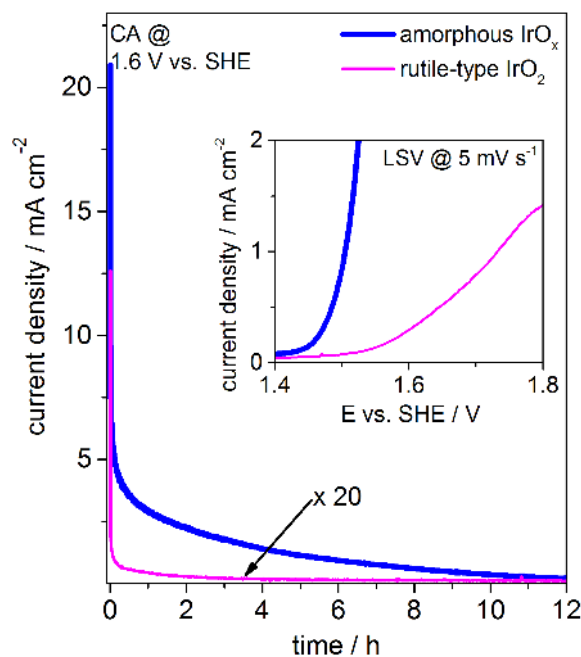


Figure 2.6: The linear sweep voltammetry (LSV) shows a much steeper and earlier OER onset for the amorphous IrO_x than for rutile-type IrO_2 .

measurements, BET surface area $2.1 \text{ m}^2 \text{ g}^{-1}$ versus $33.3 \text{ m}^2 \text{ g}^{-1}$, low versus high catalytic activity. The difference in electrocatalytic performance is of significant interest as understanding which surface species are favorable in catalyzing the OER is a prerequisite to tailor iridium oxide-based catalysts with reduced precious metal contents.

The electronic structure of these different iridium oxide powders may provide valuable insights into the nature of such active species. To characterize their electronic structures, we turn to XPS and NEXAFS.

NAP-XPS and NEXAFS

The most striking differences in the electronic structure of the two powders investigated in this work are found in their Ir 4f lines and OK-edges as illustrated in Figures 2.7 and 2.8. The Ir 4f line of the amorphous IrO_x is significantly broader than that of rutile-type IrO_2 . The difference spectrum highlights that in the amorphous IrO_x intensity is shifted away from the positions of maximum intensity in the rutile-type IrO_2 (61.7 eV and 64.7 eV) towards higher binding energy. The increased intensity at higher binding energy is indicative of the presence of additional oxygen-related species in the amorphous powder, which is corroborated by a comparison of the OK-edges of the two samples. The OK-edge of the amorphous IrO_x shows an additional resonance at 529 eV, while the intensity registered at 530 eV is reduced compared with rutile-type IrO_2 .

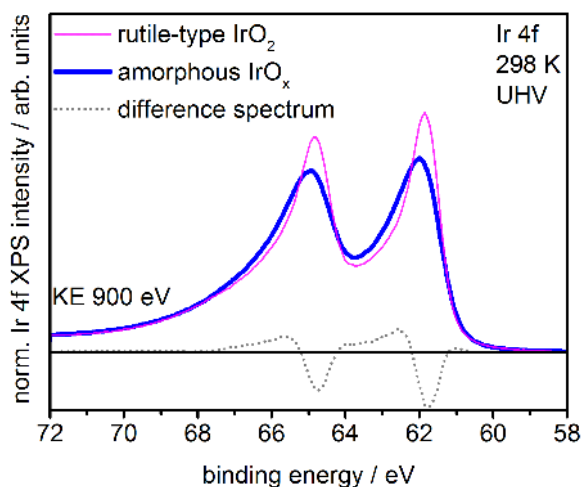


Figure 2.7: Comparison of the Ir 4f spectra of rutile-type IrO_2 and amorphous IrO_x normalized by area. The difference spectrum highlights that the amorphous IrO_x has less intensity where the rutile-type IrO_2 main lines are located at and more intensity at higher binding energy.

Although multiple species appear to be present in the amorphous powder, a specification of iridium oxides is not straightforward because of the peculiar Ir 4f line shape in these materials.¹⁶ To advance toward an identification of the species contained in the catalytically more active amorphous iridium oxide, we make use of DFT calculations. By the combination of theory and experiment, we are able to further understand the

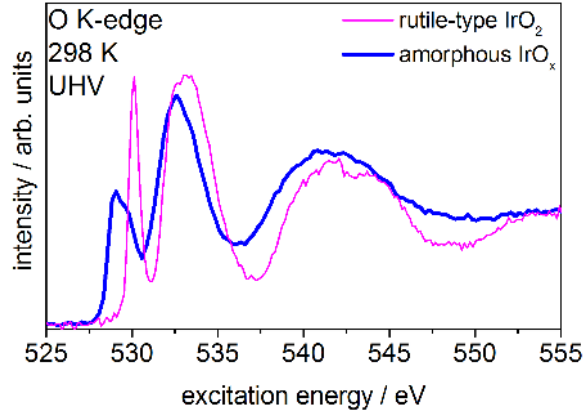


Figure 2.8: Comparison of the O K-edges of rutile-type IrO_2 and amorphous IrO_x . The amorphous IrO_x counts with an additional pre-edge feature at 529 eV and less intensity at 530 eV, where rutile IrO_2 has a sharp resonance. The broader resonance at 533 eV in rutile-type IrO_2 is shifted to slightly lower excitation energies in the amorphous IrO_x .

electronic structure of rutile-type IrO_2 and amorphous IrO_x . However, before doing so, we first benchmark our approach in Ir metal.

Single crystal Ir (111)

As XRD had shown a minor amount of Ir metal contained in the amorphous IrO_x , we found it prudent to investigate a metallic reference, for which we chose an Ir (111) single crystal. Ir single crystals have been widely studied by XPS.^{41,42} Hüfner *et al.*⁴³ determined the DS parameter, α , of Ir metal to be 0.12, which enabled a fit of the asymmetric Ir 4f spectrum with a single contribution.

As a first test of our theoretical approach, we computed the PDOS of Ir metal in a 32-atom supercell with and without an Ir 4f core hole on a single excited atom. We found that the PDOS is only weakly structured and, therefore, the Ir 4f peak shape should be fit well by a standard DS function. To illustrate this point, consider that the most prominent shake-up satellites will come from transitions from occupied states at E_F to unoccupied states slightly above E_F , as the energy dependence of the transition probability is $1/\epsilon^2$, where ϵ is the excitation energy. Thus, because the states at E_F are principally d character and the shake-up process is governed by a monopole selection rule, we expect satellites will be due to transitions from occupied to unoccupied d states. Figure 2.9 shows the d states on an Ir atom with a 4f core hole, PDOS(d). Clearly, there is no significant structure in the PDOS(d). As a result, the final states are well represented by a flat DOS, and asymptotic theory is predicted to hold.

Figure 2.10 shows the Ir 4f line of an Ir (111) single crystal at three different probing depths. As expected from the theoretical calculations, good agreement between fit

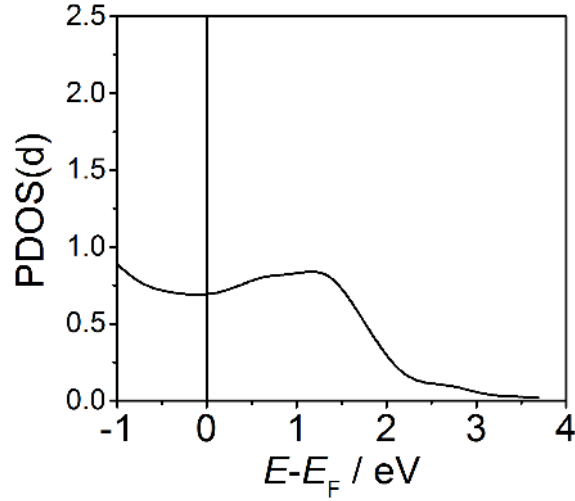


Figure 2.9: Calculated PDOS(d) of Ir metal in the presence of a 4f core hole. The PDOS shows no significant structuring.

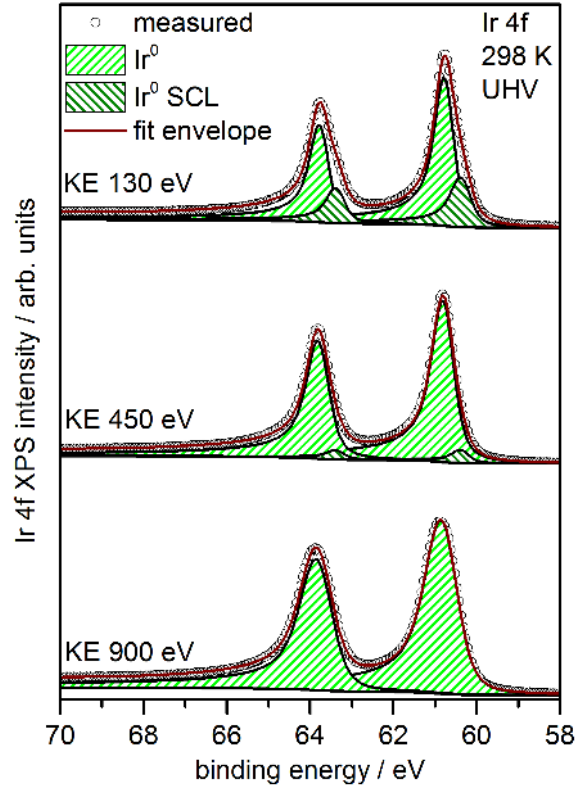


Figure 2.10: Ir 4f spectra with fits of an Ir (111) single crystal measured with three different kinetic energies (KE) of the photoelectrons. In the 130 eV and 450 eV KE spectra, the surface core levels (SCL) of the single crystal termination are visible.

and experiment is obtained on the high binding energy side of the peak maximum by using a DS function (Ir^0) for the Ir $4f_{7/2}$ (Ir $4f_{5/2}$) peak located at 60.8 eV (63.8 eV). The DS parameter α found to best fit the spectra is 0.13, which is in good agreement with the value determined by Hüfner *et al.*⁴³ On the low binding energy side of the peak

maximum, however, an additional peak (Ir^0 SCL) appears in the 130 eV and 450 eV KE spectra due to the surface core level shift (SCLS) of the single crystal surface termination. This contribution is the most pronounced in the most surface-sensitive measurement and diminishes at larger probing depths. The appearance of such an SCLS has already been reported in the literature both by theory and experiment.^{42,44} These previous studies have found an SCLS of approximately 0.5 eV on Ir (111) surfaces, slightly larger than the 0.4 eV shift we observe. However, accurate measurement of the SCLS requires a dedicated effort to ensure the surface remains clean because even small amounts of contamination, e.g. adsorbed carbonaceous species, will modify or mask this additional contribution.⁴² We further note that the $\text{Ir } 5p_{1/2}$ peak is located at a binding energy of ≈ 63 eV and completely buried by the $\text{Ir } 4f$ signal. A determination of the theoretical cross-section ratio between the $5p_{1/2}$ and $4f$ peaks based on the calculations by Yeh and Lindau⁴⁵ yields at most 2 % for the photon energies employed in this work. Hence, the $\text{Ir } 5p_{1/2}$ has such a minor contribution to the recorded spectra that we omitted it in our fits in the interest of clarity. This omission will lead to a minor broadening of the $\text{Ir } 4f$ peak contributions. The employed fit parameters are listed in Table 2.1. With higher excitation energy, the energy resolution of the beam line deteriorates. Therefore, the Gaussian contributions and the FWHM of the peaks are larger with increasing KE of the photoelectrons, and the peak maxima of the DS function are slightly shifted. Besides these adjustments, the fits remain unaltered for different probing depths.

Table 2.1: Fit parameters Ir (111) single crystal at three probing depths. KE, kinetic energy; SCL, surface core level; FWHM, full width at half maximum.

130 eV KE	$\text{Ir } 4f_{7/2}$ Ir^0	$\text{Ir } 4f_{5/2}$ Ir^0	$\text{Ir } 4f_{7/2}$ Ir^0 SCL	$\text{Ir } 4f_{5/2}$ Ir^0 SCL
line shape	DS(0.13,140) SGL(100)	DS(0.13,140) SGL(100)	DS(0.13,140) SGL(100)	DS(0.13,140) SGL(100)
area / %	44.6	29.0	16.0	10.4
FWHM / eV	0.5	0.5	0.6	0.5
binding energy / eV	60.8	63.8	60.4	63.4
450 eV KE				
line shape	DS(0.13,160) SGL(95)	DS(0.13,160) SGL(95)	DS(0.13,160) SGL(95)	DS(0.13,160) SGL(95)
area / %	53.6	40.2	3.6	2.7
FWHM / eV	0.6	0.6	0.6	0.6
binding energy / eV	60.8	63.8	60.4	63.4
900 eV KE				
line shape	DS(0.13,250) SGL(90)	DS(0.13,250) SGL(90)		
area / %	57.1	42.9		
FWHM / eV	0.9	0.9		
binding energy / eV	60.9	63.9		

Transferring this finding to our measured iridium oxides (Figure 2.7) shows that, although XRD documented the presence of metallic Ir in the amorphous IrO_x powder, neither of the two powders contains metallic Ir in the surface-near region as a peak at 60.8 eV is absent in both cases.

Rutile-type IrO_2

Rutile-type IrO_2 is a metallic conductor, and therefore, an asymmetric line shape similar to the one of metallic Ir is expected. Nevertheless to date, we know of no example of a fit for rutile-type IrO_2 that requires only one component. Earlier studies tried to explain this shortcoming by a compound such as Ir_2O_3 being present in commercially available IrO_2 powders.^{13,46} Recently, Kahk *et al.*¹⁷ described the line shape based on the Kotani model⁴⁷ and proposed that the Ir 4f peak consists of a screened and an unscreened final state. Hence, they deconvoluted the rutile-type IrO_2 Ir 4f_{7/2} line into two simple Gaussian–Lorentzian peaks. Importantly, their work showed that the uncommon line shape is inherent to the material and is not connected with stoichiometry deficiencies.

However, predicting the binding energies of a screened and an unscreened state can be cumbersome. For instance, Wertheim and Guggenheim¹⁶ predicted that the unscreened satellite would have a binding energy of ≈ 3 eV above the main line, while we find a difference of ≈ 10 eV between the computed final and initial state shifts, both of which are well above the values used in the Ir 4f deconvolution of Kahk *et al.*¹⁷ In an effort to develop a simple predictive model to capture the binding energy of the satellite peaks, we use our theoretical approach previously outlined.

To understand the nature of the Ir 4f spectrum in IrO_2 , we can again turn to the PDOS of an Ir atom with an Ir 4f core hole, which we computed in a (4x4x4) supercell of IrO_2 . The resultant PDOS(d) of the Ir atom with a core hole is shown in Figure 2.11. As with Ir metal, we only show the d states because there are few s and p states near E_F . Unlike the example of the metal, however, the d states on iridium in the oxide can be seen to be highly structured in the presence of a core hole. Inspection of the figure reveals that there is a strong narrow feature at ≈ 1 eV above E_F in the final state PDOS(d). Excitation of Fermi energy electrons to this unoccupied state will lead to a shake-up satellite at ≈ 1 eV above the main line in the Ir 4f spectrum of IrO_2 . Furthermore, the occupied states (inset in Figure 2.11) have a strong feature at ≈ 2 eV below E_F because of localized nonbonding iridium d electrons. Excitation of these electrons into the unoccupied states at 1 eV above E_F may lead to the appearance of a second satellite at ≈ 3 eV above the main line in the Ir 4f spectrum. However, because the transition probability scales as $1/\epsilon^2$ this second shake-up satellite, if visible, will be less prominent than the ≈ 1 eV

satellite. Thus, at a minimum, the IrO₂ Ir 4f line should then be fit using a standard DS function to capture the main line, for which our Δ SCF calculations predict a binding energy of 61.7 eV for the Ir 4f_{7/2}, and a Gaussian at 1 eV higher binding energy to capture the primary shake-up satellite.

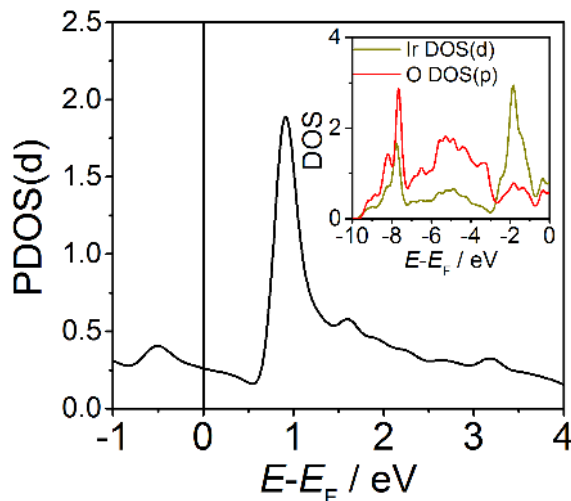


Figure 2.11: Calculated PDOS(d) of rutile-type IrO₂ in the presence of a 4f core hole. The PDOS(d) shows a sharp peak at 1 eV above E_F causing a shake-up satellite to appear 1 eV above the main line of the Ir 4f spectrum due to excitation from electrons at E_F into these unoccupied states. The inset shows the calculated occupied DOS without a core hole. The DOS has a strong feature at 2 eV binding energy. Excitation of electrons from these states into the unoccupied states 1 eV above E_F may lead to a second shake-up satellite 3 eV above the Ir 4f main line.

Based on our theoretical predictions, a least square fit of the rutile-type IrO₂ Ir 4f spectra was carried out using one DS component (Ir^{IV}) and one Gaussian satellite (Ir^{IV} sat1) for each, Ir 4f_{7/2} and Ir 4f_{5/2} (Figure 2.12). The fits at both probing depths give good agreement between the measured spectra and the fit envelopes except at a binding energy of \approx 68 eV, where a minor deviation is observed. To obtain satisfactory agreement between the fit and measurement, the second satellite (Ir^{IV} sat2) of the Ir 4f_{5/2} peak at \approx 3 eV above the main line, stemming from the excitation from the localized nonbonding Ir d states 2 eV below E_F into the unoccupied states at 1 eV above E_F (Figure 2.11), needs to be added. As the corresponding second satellite of the Ir 4f_{7/2} peak is completely buried by the Ir 4f_{5/2} main line, it was not included in the fit. The need for an additional component at around 68 eV has also been observed in previous fits of rutile-type IrO₂.⁴⁸ All fit parameters are found in Table 2.2. In contrast to the Ir single crystal measurement, no SCLS is observed in the surface-sensitive measurement of the rutile-type IrO₂ powder. The absence of the SCLS is potentially due to coverage of the surface by a carbonaceous layer.

The predominance of a single phase of IrO_2 is corroborated by the measured OK-edge. As shown in Figure 2.13, the two pronounced resonances at 530 eV and 533 eV are in good agreement with our calculations of the phase-pure rutile-type IrO_2 OK-edge, in which all oxygen and iridium are formally $\text{O}^{\text{II-}}$ and Ir^{IV} , respectively.

In summary, our combination of theory and experiment confirms that the peculiar Ir 4f line shape is inherent to rutile-type IrO_2 and not connected to the presence of additional iridium species. In general, our approach offers a predictive means of identifying the presence of satellites and their binding energies for conductive materials with structured DOSs. For example, to further test our theoretical calculations, we computed the PDOS for RuO_2 and Cu metal (not shown). For both materials, the presence (RuO_2) and the absence (Cu metal) of satellites was correctly predicted by a structured (RuO_2) and flat (Cu metal) PDOS. Finally, for the material studied in this work, iridium oxide, our approach further enables speciation of Ir 4f spectra as shown in the succeeding discussions.

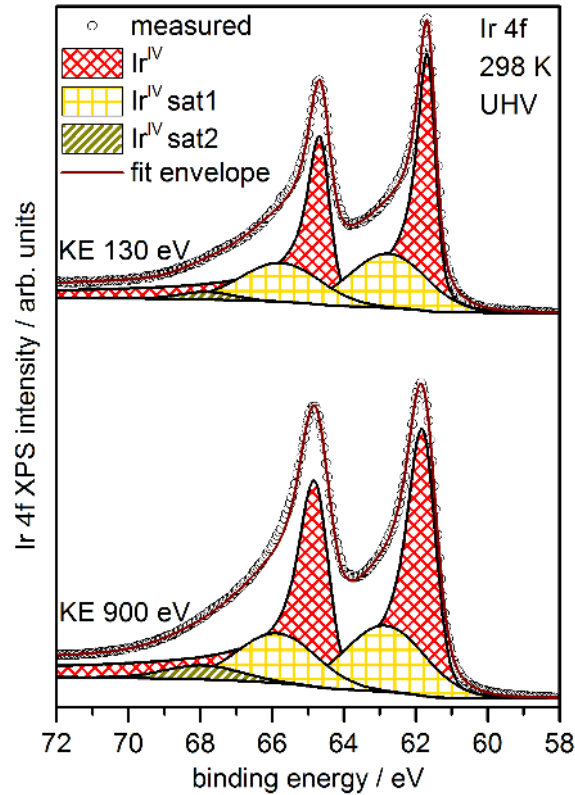


Figure 2.12: Ir 4f spectra of rutile-type IrO_2 measured at two different kinetic energies (KE) and fit with a Doniach–Šunjić main line and Gaussian satellites based on theoretical findings.

Table 2.2: Fit parameters rutile-type IrO_2 at two probing depths. KE, kinetic energy; FWHM, full width at half maximum.

130 eV KE	Ir 4f _{7/2} Ir ^{IV}	Ir 4f _{5/2} Ir ^{IV}	Ir 4f _{7/2} Ir ^{IV} sat1	Ir 4f _{5/2} Ir ^{IV} sat1	Ir 4f _{5/2} Ir ^{IV} sat2
line shape	DS(0.2,100) SGL(65)	DS(0.2,100) SGL(65)	GL(0)	GL(0)	GL(0)
area / %	44.6	34.8	11.2	8.4	1.1
FWHM / eV	0.6	0.7	2.5	2.6	1.7
binding energy / eV	61.7	64.7	62.8	65.8	67.8
900 eV KE					
line shape	DS(0.2,230) SGL(55)	DS(0.2,230) SGL(55)	GL(0)	GL(0)	GL(0)
area / %	44.1	35.7	10.4	7.8	2.1
FWHM / eV	0.9	0.9	2.6	2.6	2.5
binding energy / eV	61.8	64.8	62.9	65.9	67.9

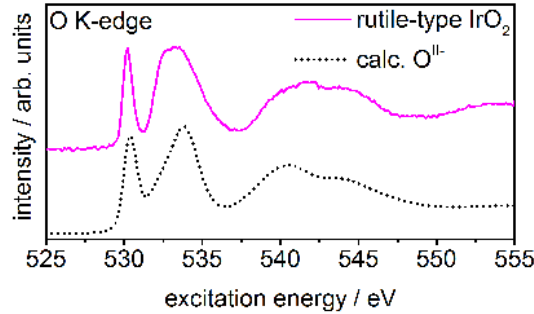


Figure 2.13: Measured (top) and calculated (bottom) O K-edge of rutile-type IrO_2 containing solely $\text{O}^{\text{II-}}$ species.

Amorphous IrO_x

As shown in Figure 2.7, the Ir 4f line shape of the amorphous powder is considerably broader than that of rutile-type IrO_2 with additional intensity appearing at higher binding energy than that of the main lines of rutile-type IrO_2 . TPR shows that the oxidation state of the amorphous sample is likely a mixture between Ir^{III} and Ir^{IV} ; hence, it is tempting to assign this additional intensity to Ir^{III} . The assignment of a higher binding energy feature to a lower oxidation state is, at first, counterintuitive in XPS. Nevertheless, in the case of silver oxides, this phenomenon is well-known.⁴⁹ In addition to this apparent defect in the cationic framework, the O K-edge of the amorphous IrO_x has a pre-edge feature at ≈ 529 eV (Figure 2.8), which hints at additional oxygen species. Such pre-edge features are commonly observed in other covalently bound oxides. By way of example, a pre-edge is observed in the O K-edge of superconducting cuprates upon doping due to the creation of holes in the O 2p orbitals (formally $\text{O}^{\text{I-}}$).^{50,51} To test if these formally Ir^{III} and $\text{O}^{\text{I-}}$ electronic defects can account for the additional features observed in the XPS and NEXAFS of IrO_x powders, we again turn to theory.

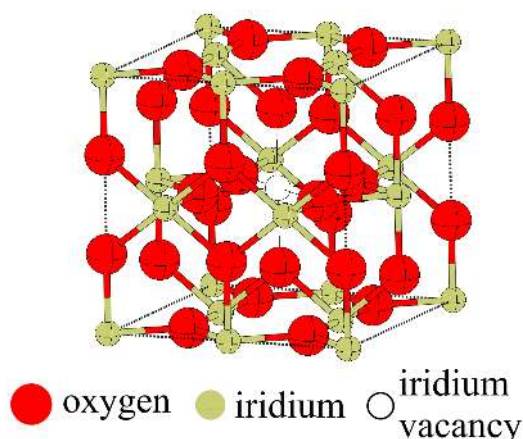


Figure 2.14: Supercell with Ir vacancy in the middle.

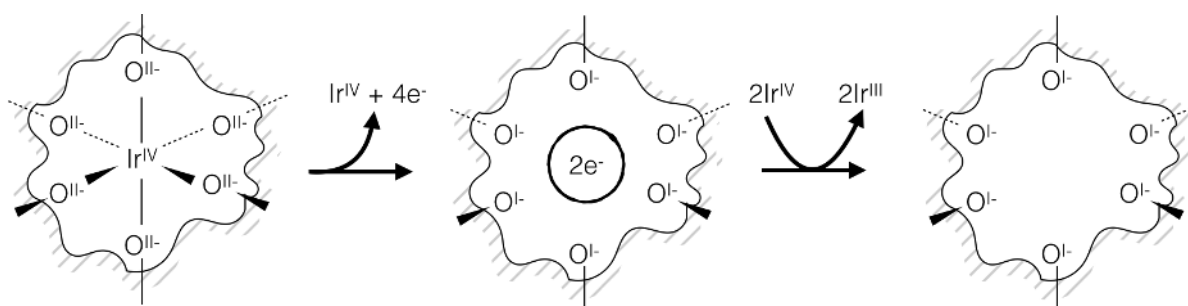


Figure 2.15: Scheme of transformations in the anionic and cationic framework upon the introduction of an Ir vacancy.

To study the possibility of O2p hole and Ir^{III} formation in IrO₂, we used a 24-atom supercell of rutile-type IrO₂ with a single Ir vacancy as a model system (Figure 2.14). As schematically outlined in Figure 2.15, introducing the Ir vacancy transforms the six formally O^{II-} anions surrounding the vacancy to formally O^{I-} species; the remaining O^{II-} anions, those not in the neighborhood of the Ir vacancy, are comparatively unaltered. Thus, six electrons are transferred from O^{II-} to the cationic framework. Of these six electrons, four are removed from the system by the Ir vacancy, Ir^{IV} and 4 e⁻. The remaining two electrons will then reduce neighboring Ir^{IV} to Ir^{III}. In support of this view, our Δ SCF calculations reveal that Ir vacancy formation does lead to the appearance of species with an Ir 4f binding energy of 62.2 eV, which we attribute to the formally Ir^{III} cations. Inspection of the PDOS(d) (not shown) reveals that these Ir^{III} are expected to have a satellite at ≈ 1 eV higher binding energy in the Ir 4f spectrum, leading to the fit shown in Figure 2.16. Evidence for the formally O^{I-} species can be found in the computed O K-edge spectrum, where the O^{I-} species introduce a strong resonance at ≈ 529 eV (Figure 2.17), in good agreement with experiment.

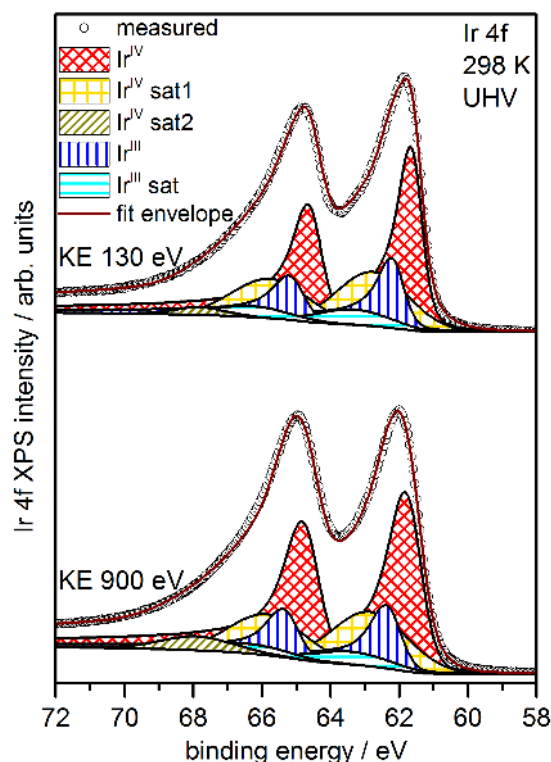


Figure 2.16: Ir 4f spectra of amorphous IrO_x measured at two different kinetic energies (KE) with Ir^{IV} and Ir^{III} Doniach–Šunjić main lines and corresponding Gaussian satellites based on theoretical findings.

Based on our theoretical findings, we developed a fit for the Ir 4f line of amorphous IrO_x , which is shown for two probing depths in Figure 2.16. We employed the established Ir^{IV} fit functions from rutile-type IrO_2 and added the Ir^{III} components found in our model calculations with DS functions (62.3 eV and 65.3 eV) and corresponding Gaussian satellites. To account for a less regular order in the amorphous sample when compared with the crystalline one, we chose a higher FWHM value for the DS components of Ir^{IV} . The separation between Ir^{IV} and Ir^{III} leading to the best fit is 0.56 eV, which is slightly larger than what our calculations predict. When taking into account both the intensities of the main lines and corresponding satellites, the fits show that the subsurface region of the amorphous IrO_x powder contains roughly 80 % Ir^{IV} and 20 % Ir^{III} species. At the outmost surface (130 eV KE measurement), the defect density is slightly ($\approx 5\%$) larger. The fit parameters of all peaks and their intensities can be found in Table 2.3.

Table 2.3: Fit parameters amorphous IrO_x as received at two probing depths. KE, kinetic energy; FWHM, full width at half maximum.

130 eV KE	Ir 4f _{7/2} Ir ^{IV}	Ir 4f _{5/2} Ir ^{IV}	Ir 4f _{7/2} Ir ^{IV} sat1	Ir 4f _{5/2} Ir ^{IV} sat1	Ir 4f _{5/2} Ir ^{IV} sat2	Ir 4f _{7/2} Ir ^{III}	Ir 4f _{5/2} Ir ^{III}	Ir 4f _{7/2} Ir ^{III} sat1	Ir 4f _{5/2} Ir ^{III} sat1
line shape	DS(0.2,100) SGL(50)	DS(0.2,100) SGL(50)	GL(0)	GL(0)	GL(0)	DS(0.2,100) SGL(50)	DS(0.2,100) SGL(50)	GL(0)	GL(0)
area / %	32.6	24.8	8.2	6.2	0.8	13.4	10.1	2.3	1.7
FWHM / eV	0.8	0.9	2.5	2.6	1.8	0.9	1	2.4	2.6
binding en- ergy / eV	61.7	64.7	62.8	65.8	67.8	62.3	65.3	63.3	66.3
900 eV KE	DS(0.2,230) SGL(45)	DS(0.2,230) SGL(45)	GL(0)	GL(0)	GL(0)	DS(0.2,230) SGL(45)	DS(0.2,230) SGL(45)	GL(0)	GL(0)
line shape	DS(0.2,230) SGL(45)	DS(0.2,230) SGL(45)	GL(0)	GL(0)	GL(0)	DS(0.2,230) SGL(45)	DS(0.2,230) SGL(45)	GL(0)	GL(0)
area / %	33.8	27.4	7.9	6.0	2.0	10.9	8.8	1.9	1.4
FWHM / eV	1.1	1.1	2.6	2.6	2.5	1	1.1	2.6	2.6
binding en- ergy / eV	61.8	64.8	62.9	65.9	67.9	62.4	65.4	63.4	66.4

The OK-edge of the amorphous IrO_x has resonances at 529 eV and 530 eV. Hence, our calculations predict that it contains both formally $\text{O}^{\text{I}-}$ and $\text{O}^{\text{II}-}$ species. Because the O 2p hole is a localized defect, we can take a linear combination of the computed OK-edge spectra of $\text{O}^{\text{I}-}$ and $\text{O}^{\text{II}-}$ to estimate the amount of $\text{O}^{\text{I}-}$ in the probing depth of the experiment. Doing so, we find that a spectrum with approx. 40 % $\text{O}^{\text{I}-}$ and 60 % $\text{O}^{\text{II}-}$ results in a good agreement between measurement and theory (Figure 2.17).

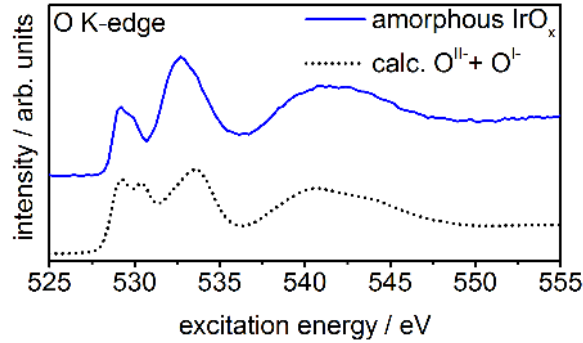


Figure 2.17: Measured (top) and calculated (bottom) O K-edge of amorphous IrO_x containing both $\text{O}^{\text{I}-}$ and $\text{O}^{\text{II}-}$ species. For the calculated spectrum a share of 40 % $\text{O}^{\text{I}-}$ yielded the best agreement with the measured spectrum.

In the model outlined in Figure 2.15, per each one Ir^{III} , three $\text{O}^{\text{I}-}$ are created. In line with this prediction, we find a higher concentration of electronic defects in the anionic than in the cationic framework of the amorphous material. A ratio as high as 1:3, though, does not result. This observation shows that as expected, the atomic structure of the amorphous IrO_x will be more complex than our model system. Nevertheless, the local defects in the atomic structure present in our model capture both kinds of

electronic defects observed in the amorphous IrO_x . Hence, these types of local defects are likely to be present in the amorphous framework. Furthermore, the calculations and fits based thereon allow us to estimate the defect concentrations in the surface and subsurface region, which are probed by XPS/NEXAFS and likely crucial for heterogeneous catalytic reactions.

In situ XRD, XPS, and NEXAFS

To substantiate our proposed fit for the amorphous IrO_x , we performed *in situ* XRD and XPS/NEXAFS heating experiments of the powder. In XRD, we already know that the initial pattern shows only broad peaks, compare Figure 2.2. Upon heating, the pattern in Figure 2.18 starts to show rutile-type IrO_2 reflections at 623 K. Crystallization appears to start roughly at this temperature under 10^5 Pa in synthetic air as we had similarly observed in DSC. When heating to higher temperatures, the reflections become sharper hinting at a higher degree of homogeneity of the sample with increasing temperature.

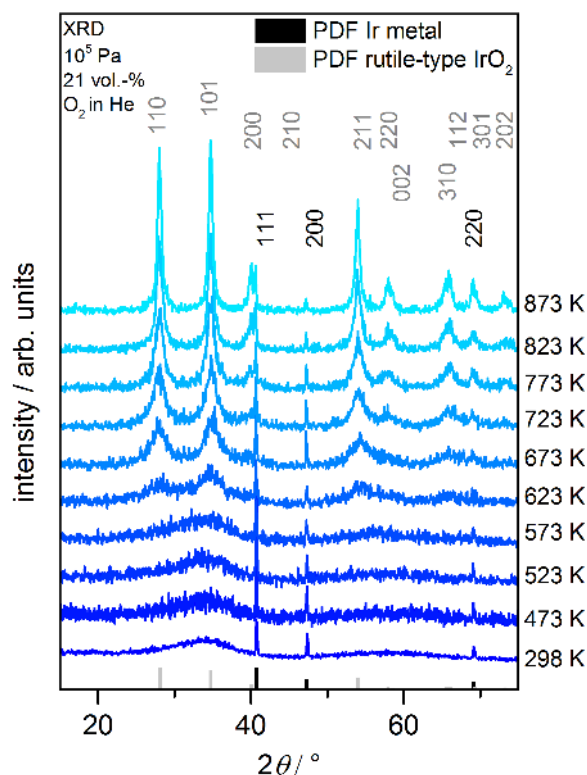


Figure 2.18: *In situ* XRD heating experiment at 10^5 Pa in 21 vol.% O_2 of amorphous powder that initially does not show rutile-type IrO_2 reflections but only metallic ones. Upon heating, rutile-type IrO_2 reflections evolve.

In both XPS and NEXAFS, the changes in the spectra upon heating in 25 Pa O_2 are obvious (Figures 2.19 and 2.20). The contributions of Ir^{III} to the Ir 4f line at 62.3 eV

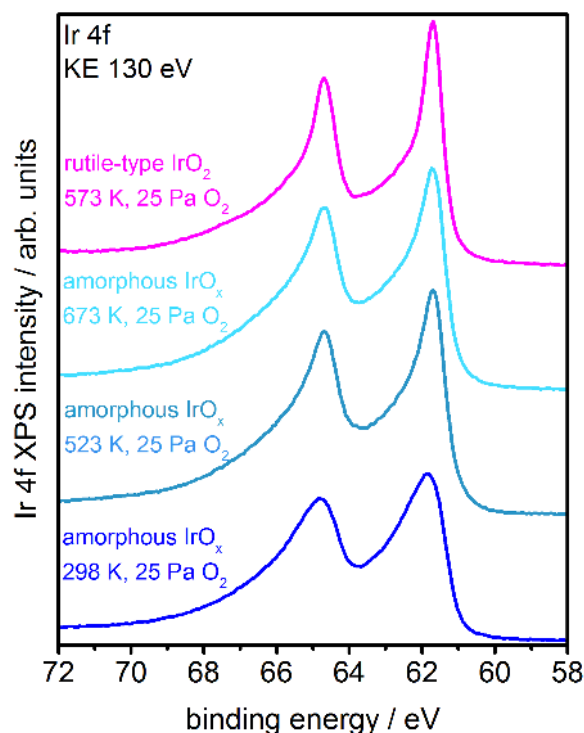


Figure 2.19: *In situ* XPS heating experiment of the amorphous powder. The intensity at higher binding energy than the main line of IrO_2 is reduced with increasing temperature. A comparison with the rutile-type IrO_2 Ir 4f spectrum and the measurement of the amorphous IrO_x at 673 K still shows a slightly broader spectrum.

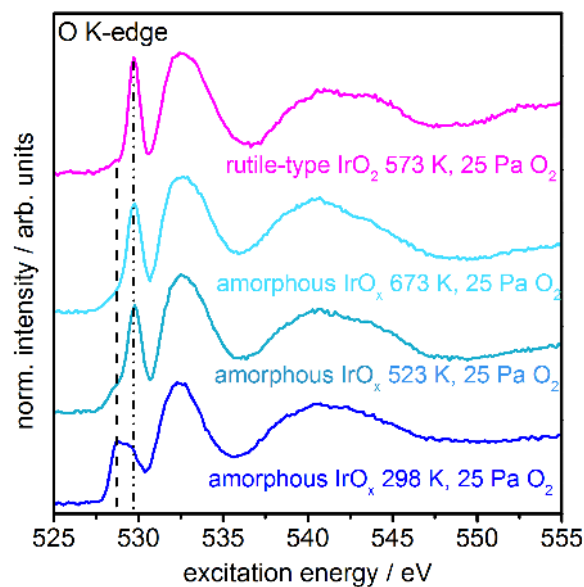


Figure 2.20: *In situ* NEXAFS heating experiment of the amorphous IrO_x powder. Spectra are corrected by the O_2 gas phase transmission. The intensity of the resonance at 529 eV is reduced with increasing temperature. A comparison with the rutile-type IrO_2 O K-edge still shows that a slightly larger contribution of the 529 eV resonance is still present at 673 K.

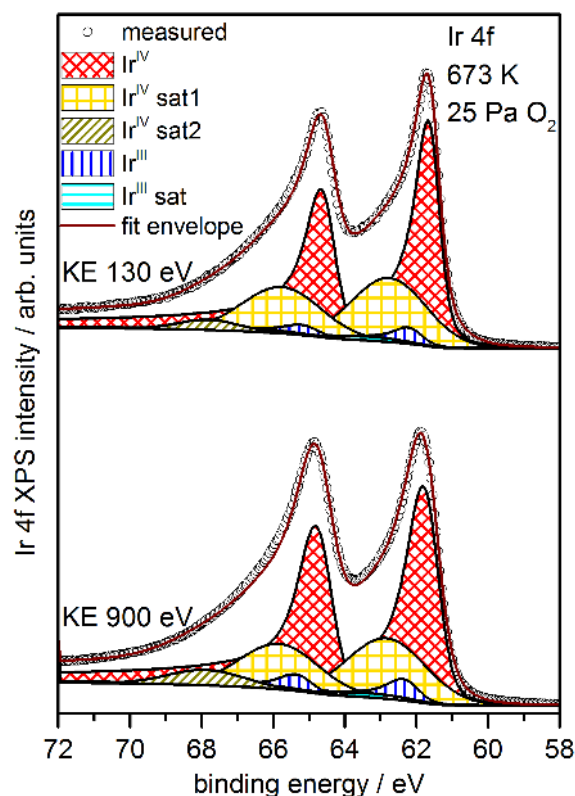


Figure 2.21: Ir 4f spectra of amorphous IrO_x measured at 673 K in 25 Pa O_2 at two different kinetic energies (KE) with theory-based fit models. Compared with the measurement at room temperature, the Ir^{III} component is decreased.

and 65.3 eV are reduced with a concomitant decrease in the intensity of the 529 eV component in the OK-edge and an increase in the intensity of the resonance at 530 eV. To remove the distortion of the NEXAFS spectra by photon absorption in the gas phase, the spectra shown in Figure 2.20 were reconstructed by taking into account the O_2 gas phase transmission as described in detail in Hävecker *et al.*²² At 673 K, a comparison with spectra of phase pure rutile-type IrO_2 still shows discrepancies, which are likely a result of the incomplete oxidation and crystallization under the applied conditions (Figure 2.20). This view is further supported by the aforementioned observation from *in situ* XRD that heating to 673 K might not be sufficient to obtain a homogeneous sample (Figure 2.18). Therefore, a fraction of the structural and electronic defects might still be present in the IrO_x sample after heating.

The continued presence of electronic defects in the cationic framework is corroborated by a fit of the Ir 4f region. Figure 2.21 shows the fit of the Ir 4f line measured at 673 K in O_2 based on the model developed in this section. Note that the area ratio between the DS lines and the corresponding satellites is fixed to a constant value to ensure comparability between different fits. Fit parameters are listed in Table 2.4. As anticipated, the contribution of Ir^{III} is smaller than for the sample in the as-received state

(7 % vs. 20 %) but has still not completely vanished. The Ir^{IV} component increases and, as a result of partial crystallization, is more ordered than in the initial state, which is reflected by a slightly decreased FWHM even though measured at an elevated temperature. Also for this state of the powder, good agreement is obtained for the measured spectra and the fit using our newly introduced model.

Table 2.4: Fit parameters amorphous IrO_x at 673 K in 25 Pa O_2 at two probing depths. KE, kinetic energy; FWHM, full width at half maximum.

130 eV KE	Ir 4f _{7/2} Ir ^{IV}	Ir 4f _{5/2} Ir ^{IV}	Ir 4f _{7/2} Ir ^{IV} sat1	Ir 4f _{5/2} Ir ^{IV} sat1	Ir 4f _{5/2} Ir ^{IV} sat2	Ir 4f _{7/2} Ir ^{III}	Ir 4f _{5/2} Ir ^{III}	Ir 4f _{7/2} Ir ^{III} sat1	Ir 4f _{5/2} Ir ^{III} sat1
line shape	DS(0.2,100) SGL(55)	DS(0.2,100) SGL(55)	GL(0)	GL(0)	GL(0)	DS(0.2,100) SGL(55)	DS(0.2,100) SGL(55)	GL(0)	GL(0)
area / %	41.2	32.1	10.3	7.9	1.3	3.5	2.6	0.6	0.4
FWHM / eV	0.8	0.9	2.5	2.6	2	0.9	1	2.3	2.4
binding energy / eV	61.7	64.7	62.8	65.8	67.8	62.3	65.3	63.3	66.3
900 eV KE	Ir 4f _{7/2} Ir ^{IV}	Ir 4f _{5/2} Ir ^{IV}	Ir 4f _{7/2} Ir ^{IV} sat1	Ir 4f _{5/2} Ir ^{IV} sat1	Ir 4f _{5/2} Ir ^{IV} sat2	Ir 4f _{7/2} Ir ^{III}	Ir 4f _{5/2} Ir ^{III}	Ir 4f _{7/2} Ir ^{III} sat1	Ir 4f _{5/2} Ir ^{III} sat1
line shape	DS(0.2,230) SGL(50)	DS(0.2,230) SGL(50)	GL(0)	GL(0)	GL(0)	DS(0.2,230) SGL(50)	DS(0.2,230) SGL(50)	GL(0)	GL(0)
area / %	40.2	32.6	9.5	7.1	2.3	4.0	3.2	0.7	0.5
FWHM / eV	1	1.1	2.6	2.6	2.5	1	1.1	2.6	2.6
binding energy / eV	61.8	64.8	62.9	65.9	67.9	62.4	65.4	63.4	66.4

Conclusion

In conclusion, we describe the electronic structure of Ir metal, rutile-type IrO_2 , and an amorphous IrO_x . We confirm that the line shape of Ir metal is well-described by a simple DS function. For iridium oxides, however, a shake-up satellite is identified at 1 eV above the main Ir 4f line. This satellite accounts for the peculiar line shape of phase-pure rutile-type IrO_2 . As we have probed our samples at different information depths, we can exclude that the observed phenomena are solely due to surface effects but are also present in the subsurface region. Our theoretical models explain formerly unidentified features observed in the O K-edge and the Ir 4f line of amorphous IrO_x . O 2p hole states, which are formally $\text{O}^{\text{I-}}$, cause a resonance at 529 eV in the O K-edge NEXAFS. A compensatory Ir^{III} species exhibits a reverse binding energy shift in XPS. This reverse shift is responsible for the increased intensity in the Ir 4f line at higher binding energy than the rutile-type IrO_2 Ir 4f signal. Hence, our calculations show that caution is required when assigning oxidation states based solely on binding energy shifts. Finally, our investigation enables an estimation of the concentration of the electronic

defects in the anionic and cationic framework of the more active catalyst studied in this work. These electronic defects may account for the increased electrocatalytic activity observed in such amorphous iridium oxide systems. For a deeper understanding of how such highly defective termination layers evolve on surfaces under the influence of applied potentials, XPS and NEXAFS investigations of oxygen-evolving iridium catalysts are needed.

Supplementary Information[¶]

Calculated PDOS and measured valence band spectra

To further investigate the differences in the electronic structure of rutile-type IrO_2 , amorphous IrO_x , and the contained $\text{O}^{\text{I}-}$ and $\text{O}^{\text{II}-}$ species, we explored the occupied electronic states of the materials near the Fermi energy (E_{F}) by comparing measured valence band (VB) spectra with the computed projected density of states (PDOS). Though the PDOS and VB spectra are not exactly comparable because of, for instance, matrix element effects and lifetime broadening, the main peak positions should still be in good agreement. By using a projected density of states, it is possible to extract information about which element gives rise to the states associated with a given peak, making a combination of the measured VB spectra and the computed PDOS an excellent complement to the OK-edge NEXAFS, which effectively measures the unoccupied part of the projected O p states, PDOS(p).

The calculations were performed using the cells shown in Figures 2.1 and 2.14. The geometry of the three iridium atoms surrounding one oxygen atom in the defect-free IrO_2 cell is shown in Figure S2.7.1. In the cell that contains an Ir vacancy, for six of the oxygen atoms one of these surrounding iridium atoms is missing.

Figure S2.7.2 shows a comparison of the PDOS of only the $\text{O}2p_y$ and all O 2p orbitals of single $\text{O}^{\text{I}-}$ and $\text{O}^{\text{II}-}$ species, respectively. The $\text{O}2p_y$ orbitals are those mainly involved in π -bonding and -anti-bonding as may be inferred from Figure S2.7.1. Their PDOS is shown separately since we observe a shift of these states towards more positive energies, i. e. a deoccupation, when comparing $\text{O}^{\text{I}-}$ and $\text{O}^{\text{II}-}$. This deoccupation is also reflected by an increased splitting of the overall PDOS of the O 2p states near E_{F} of $\text{O}^{\text{I}-}$ when compared to $\text{O}^{\text{II}-}$.

[¶]This section was partly reproduced from the Supplementary Information to Pfeifer, V., Jones, T. E., Velasco Vélez, J. J., Massué, C., Greiner, M. T., Arrigo, R., Teschner, D., Girgsdies, F., Scherzer, M., Allan, J., Hashagen, M., Weinberg, G., Piccinin, S., Hävecker, M., Knop-Gericke, A., and Schlögl, R. **2016** The electronic structure of iridium oxide electrodes active in water splitting. *Phys. Chem. Chem. Phys.*, 18, 2292–2296, doi: 10.1039/C5CP06997A with permission from the PCCP Owner Societies.

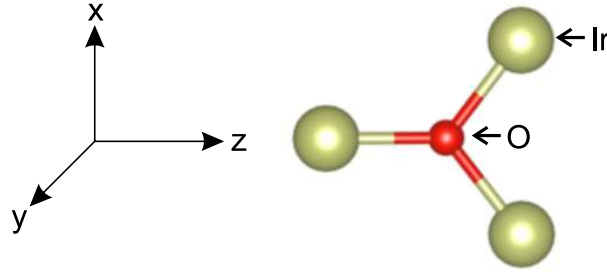


Figure S2.7.1: Geometry of the three iridium atoms surrounding one oxygen atom in the defect free IrO_2 cell. The Ir and O atoms are in the xz -plane

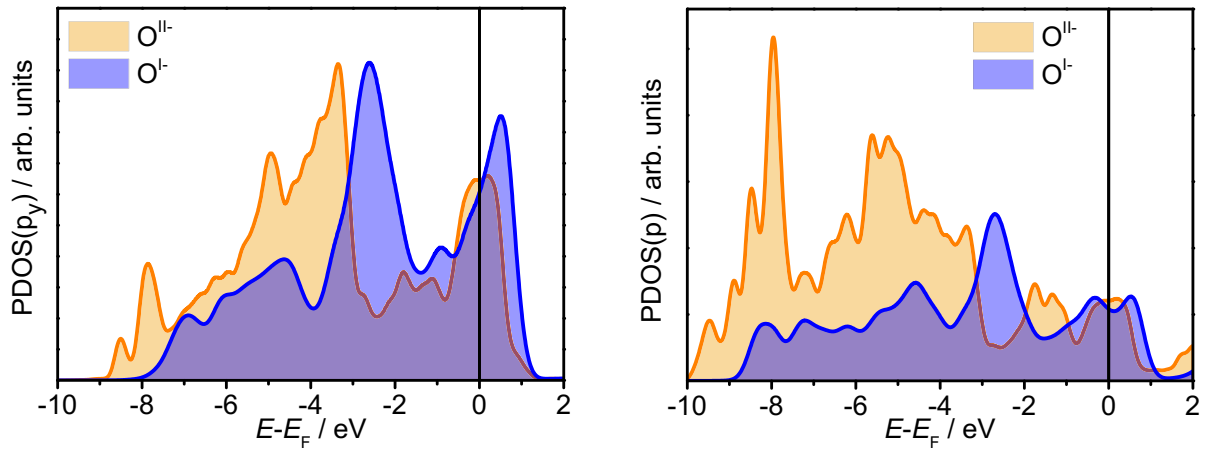


Figure S2.7.2: Projected density of states of (left) $\text{O}2p_y$ and (right) all $\text{O}2p$ orbitals for $\text{O}^{\text{I}-}$ and $\text{O}^{\text{II}-}$ species.

Figures S2.7.3 and S2.7.4 show comparisons of all Ir 5d and O 2p states calculated for the entire rutile-type IrO_2 cell without (see Figure 2.1) and with (see Figure 2.14) Ir vacancy. Introduction of the Ir vacancy leads to the creation of $\text{O}^{\text{I}-}$ and Ir^{III} . While the increased splitting of the O 2p orbitals near E_F may still be seen, it is significantly washed out when compared to the presentation in Figure S2.7.2 for only single $\text{O}^{\text{I}-}$ and $\text{O}^{\text{II}-}$ species.

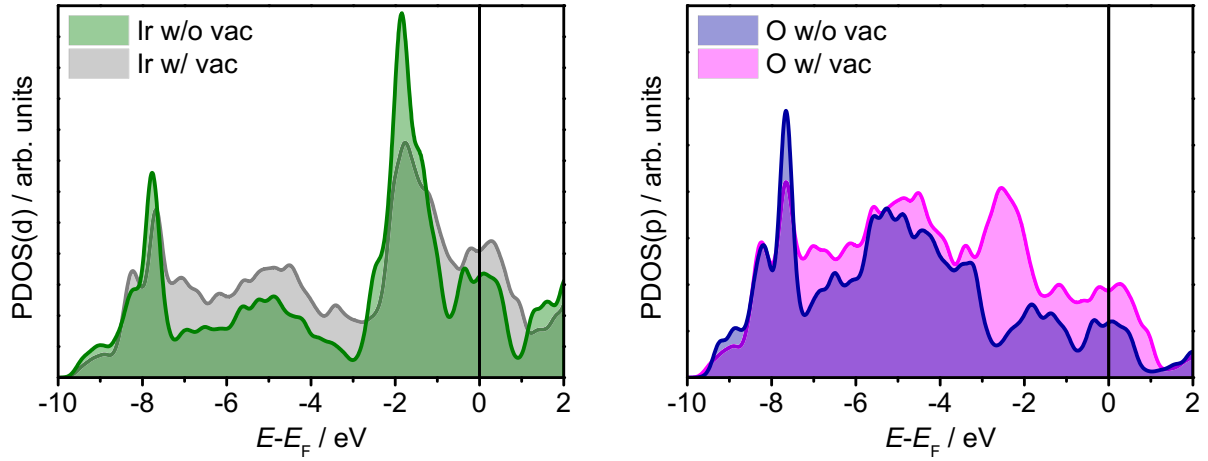


Figure S2.7.3: Projected density of states of all (left) Ir 5d and (right) O 2p orbitals for rutile-type IrO_2 without and with Ir vacancy, calculated using cells shown in Figures 2.1 and 2.14.

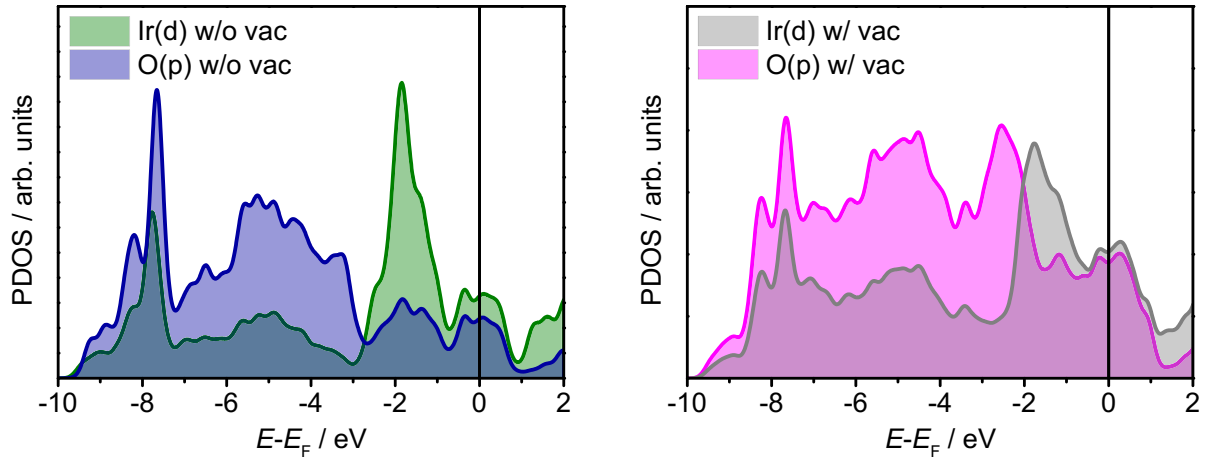


Figure S2.7.4: Projected density of states of all Ir 5d and O 2p orbitals for rutile-type IrO_2 without (left) and with (right) Ir vacancy, calculated using cells shown in Figures 2.1 and 2.14.

Figure S2.7.5 shows a comparison of the measured valence bands and oxygen K-edges of rutile-type IrO_2 and amorphous IrO_x . It may be seen that the valence band of amorphous IrO_x has reduced intensity at 2 eV and 0.5 eV binding energy when compared to the prominent features in the rutile-type IrO_2 at these energies. The intensity loss near E_F may allude to the deoccupation of O 2p states and the formation of additional O 2p hole states as suggested by the PDOS of O^{1-} (see Figure S2.7.2). Nevertheless, since the valence band consists of contributions of both the Ir 5d and the O 2p states, it is rather difficult to explicitly disentangle the respective contributions. However, when we consider the element-specific NEXAFS OK-edge of amorphous IrO_x , we are indeed able to confirm the deoccupation of O 2p states and the presence

of additional O 2p hole states in amorphous IrO_x by an additional resonance at 529 eV that is absent in rutile-type IrO₂. Therefore, monitoring the element-specific O K-edge presents a more direct and unequivocal way of observing the deoccupation of electronic states near E_F than the unspecific valence band measurements. Techniques to investigate changes in the occupied states near E_F in future investigations may be element-specific X-ray emission spectroscopies.

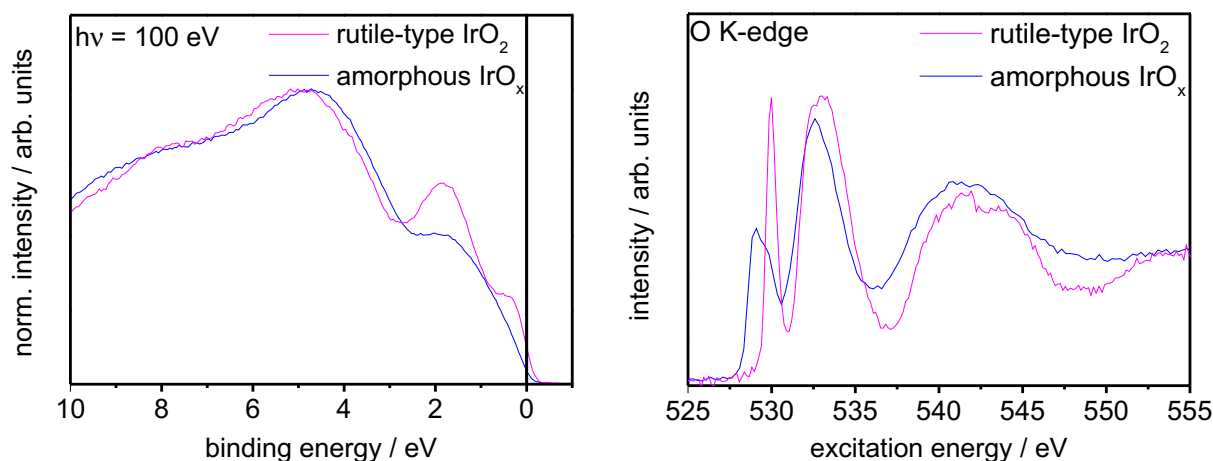


Figure S2.7.5: (left) Comparison of the measured valence band spectra of rutile-type IrO₂ and amorphous IrO_x normalized by maximum intensity. (right) Comparison of the O K-edges of rutile-type IrO₂ and amorphous IrO_x.

Literature survey of Ir 4f line shape interpretations

The Ir 4f line shape of iridium oxides and species contained in different types of iridium oxide have been heavily discussed in literature. The intrinsic asymmetric shape of stoichiometric rutile-type IrO₂ was interpreted by Wertheim *et al.*¹⁶ as well as Kahk *et al.*¹⁷ Wertheim *et al.* do a full many body calculation of the line shape expected for rutile-type IrO₂ while Kahk *et al.* reason their proposed screened and unscreened states by the Kotani model.⁴⁷ Although Wertheim *et al.* predicted that in such an approach the unscreened state would have a binding energy ≈ 3 eV above the main line, Kahk *et al.*'s fits use significantly lower values (≈ 0.6 eV).

Table S2.7.1 gives a general overview of previously published XPS studies on iridium oxides (including both crystalline and amorphous forms) and one reference for IrCl₃ with the proposed line shapes, contained species, and binding energy positions. In general, for rutile-type IrO₂ powders most literature findings agree on an Ir 4f_{7/2} binding energy value of 61.7 eV - 61.9 eV for Ir^{IV}. Only Hara *et al.*⁴⁶ claim to have a considerable amount of Ir^{III} in commercially available IrO₂ powder and suggest a binding energy of 62 eV for Ir^{III} and 63.7 for Ir^{IV}. Similarly, Augustynski *et al.*⁵² attribute a bind-

ing energy of 61.6 eV to Ir^{III} in a compound of Ir₂O₃, for which no crystallographic data is available, though, and a binding energy of 62.7 eV to Ir^{IV} in IrO₂.

Several groups deconvoluted the recorded Ir 4f spectra and proposed a wealth of different line shapes and interpretations of present Ir species.^{8,12,14,17,46,48,52} Especially the spectra of anodized iridium and of iridium oxyhydroxides were found to be broader and therefore suspected to contain more species than those of rutile-type IrO₂.

By way of example, Augustynski *et al.*⁵² fitted an additional peak at 1.6 eV above the main line of rutile-type IrO₂ and attributed this to Ir^{VI}, which they suggested to be present in commercially available IrO₂ due to surface oxidation. Similarly, Atanasoska *et al.*⁴⁸ fitted peaks at 1.4 eV and 6.3 eV above the main line of rutile-type IrO₂. These additional features have similar binding energies as those of the fit proposed in this work. However, in Atanasoska *et al.*'s⁴⁸ fits, symmetric line shapes were used for the main line, which is unexpected for metallic conductors. In addition, they ascribed the peak seen at 1.4 eV above the main line to Ir in an oxidation state of higher than IV, whereas we show in this work that the feature \approx 1 eV above the main line is a shake-up satellite of Ir^{IV} species. Furthermore, Casalongue *et al.*¹⁴ assign an oxidation state of V to species appearing during OER at 0.7 eV above their asymmetric main line. This assignment encouraged Nong *et al.*⁸ to also mention that the species they observe at higher binding energy after OER might be Ir with an oxidation state higher than IV. Finally, Kim *et al.*⁵³ also discussed about the presence of Ir^{VI} on anodized Ir electrodes since they observed intensity at binding energies 2.5 eV above the main line. This small literature overview already witnesses the large discrepancies between the interpretation of different Ir 4f spectra.

It needs to be noted that all assignments of iridium oxidation states higher than IV were simply based on shifts of these components to higher binding energies, although Kötze *et al.*⁶ and Hall *et al.*¹² had pointed out that there might be no correlation between a higher oxidation state and a higher binding energy of iridium species. In line with this advice, the Ir 4f binding energy of IrCl₃, with Ir in oxidation state III, was found to be at higher values than those of rutile-type IrO₂ with Ir in oxidation state IV (62.6 eV vs. 61.8 eV). Due to the lack of a well-defined reference material with Ir in oxidation state V, such a material could not be characterized via XPS.

In the present study of the OER-active X-ray amorphous IrO_x, neither from our TPR measurements nor from the charge balance in the employed defect model we see evidence for the presence of Ir^V but only for Ir^{III}, which is why we attribute the additional peak located 0.6 eV above the main line of Ir^{IV} to Ir^{III} species.

Table S2.7.1: Literature values of Ir4f_{7/2} binding energies of IrO_x and IrCl₃. Fit shape abbreviations: GL:Gaussian-Lorentzian, G-DS: Gaussian convoluted Doniach-Šunjić, BE: binding energy

	sample type	BE/ eV	type/ fit shape	BE/ eV	type/ fit shape	BE/ eV	type/ fit shape
Atanasoska <i>et al.</i> ⁴⁸	IrO ₂ (thermal decomposition IrCl ₃)	61.2	Ir ^{IV} /GL	62.6	Ir ^{>IV} /GL	67.5	unknown/GL
Augustynski <i>et al.</i> ⁵²	IrO ₂	62.7	Ir ^{IV} /GL	64.3	Ir ^{VI} /GL		
	Ir ₂ O ₃	61.6	Ir ^{III} /GL				
	anodic IrO _x	62.9	Ir ^{IV} /GL	64.3	Ir ^{VI} /GL		
Casalongue <i>et al.</i> ¹⁴	Ir ^{IV} oxide nanoparticles	61.5	Ir ^{IV} /G-DS	62.2	Ir ^V (only present during OER)/G-DS		
Hall <i>et al.</i> ¹²	anodic IrO _x	61.2	Ir ^{IV} /GL	63.1	oxide-hydroxide/GL		
Hara <i>et al.</i> ⁴⁶	IrO ₂ powder	62	Ir ^{III} /not specified	63.7	Ir ^{IV} /not specified		
Kahk <i>et al.</i> ¹⁷	IrO ₂ powder	61.7	Ir ^{IV} screened/GL	62.4	Ir ^{IV} unscreened/GL	74.5	satellite/GL
Kim <i>et al.</i> ⁵³	IrO ₂ powder / anodized Ir electrode	61.9	Ir ^{IV} /no fit	63.4	Ir ^{VI} /no fit		
Kötz <i>et al.</i> ⁶	IrO ₂ (reactively sputtered)	61.8	Ir ^{IV} no fit				
	anodic IrO _x	62.4	not specified/no fit				
Peuckert <i>et al.</i> ¹³	IrO ₂ (thermally oxidized Ir)	61.9	Ir ^{IV} /no fit				
	anodic IrO _x	61.2	not specified/no fit				
Wertheim <i>et al.</i> ¹⁶	IrO ₂ single crystal	61.6	Ir ^{IV} /calculated asym.				
Folkesson ⁵⁴	IrCl ₃	62.6	Ir ^{III}				

An alternative technique to monitor the oxidation state of Ir is X-ray absorption spectroscopy, which several groups have used *in situ* to relate changes in the white line of the Ir L-edge with the present Ir oxidation state.^{55–57} For electrodeposited, hydrated Ir oxyhydroxide films, it was observed that the white line is broadened and shifted to higher excitation energies with increased potential. In comparison with reference compounds (IrO_2 and IrCl_3), these results were interpreted as to initially have Ir in oxidation states III and IV and to later have in addition Ir in an oxidation state of up to V present during OER. All these studies restricted their investigations to monitoring changes in the metal states, whereas possible changes in their environment, hence the oxygen states, were not considered.

Acknowledgments

The authors acknowledge BESSY II/HZB for granting beam time at the ISSS beam line under the proposal #14201159 and support during measurements.

References

- [1] J. P. Barton, D. G. Infield, *IEEE T. Energy Conver.* **2004**, 19, 441.
- [2] C. C. L. McCrory, S. Jung, J. C. Peters, T. F. Jaramillo, *J. Am. Chem. Soc.* **2013**, 135, 16977.
- [3] M. Carmo, D. L. Fritz, J. Mergel, D. Stolten, *Int. J. Hydrogen Energy* **2013**, 38, 4901.
- [4] A. Damjanovic, A. Dey, J. O. M. Bockris, *J. Electrochem. Soc.* **1966**, 113, 739.
- [5] S. Trasatti, *J. Electroanal. Chem. Interfacial Electrochem.* **1980**, 111, 125.
- [6] R. Kötz, H. Neff, S. Stucki, *J. Electrochem. Soc.* **1984**, 131, 72.
- [7] D. N. Buckley, L. D. Burke, *J. Chem. Soc., Faraday Trans. 1* **1975**, 71, 1447.
- [8] H. N. Nong, H.-S. Oh, T. Reier, E. Willinger, M.-G. Willinger, V. Petkov, D. Teschner, P. Strasser, *Angew. Chem. Int. Ed.* **2015**, 54, 2975.
- [9] M. Bernicke, E. Ortel, T. Reier, A. Bergmann, J. Ferreira de Araújo, P. Strasser, R. Kraehnert, *ChemSusChem* **2015**, 8, 1908.
- [10] T. Reier, D. Teschner, T. Lunkenbein, A. Bergmann, S. Selve, R. Kraehnert, R. Schlögl, P. Strasser, *J. Electrochem. Soc.* **2014**, 161, F876.
- [11] R. Kötz, H. J. Lewerenz, P. Brüesch, S. Stucki, *J. Electroanal. Chem. Interfacial Electrochem.* **1983**, 150, 209.
- [12] Y. H. Hall, P. M. A. Sherwood, *J. Chem. Soc., Faraday Trans. 1* **1984**, 80, 135.
- [13] M. Peuckert, *Surf. Sci.* **1984**, 144, 451.
- [14] H. G. Sanchez Casalongue, M. L. Ng, S. Kaya, D. Friebe, H. Ogasawara, A. Nilsson, *Angew. Chem. Int. Ed.* **2014**, 53, 7169.
- [15] S. K. Panda, S. Bhowal, A. Delin, O. Eriksson, I. Dasgupta, *Phys. Rev. B* **2014**, 89, 155102.
- [16] G. K. Wertheim, H. J. Guggenheim, *Phys. Rev. B* **1980**, 22, 4680.
- [17] J. M. Kahk, C. G. Poll, F. E. Oropeza, J. M. Ablett, D. Céolin, J.-P. Rueff, S. Agrestini, Y. Utsumi, K. D. Tsuei, Y. F. Liao, F. Borgatti, G. Panaccione, A. Regoutz, R. G. Egdell, B. J. Morgan, D. O. Scanlon, D. J. Payne, *Phys. Rev. Lett.* **2014**, 112, 117601.

- [18] L. Atanasoska, P. Gupta, C. Deng, R. Warner, S. Larson, J. Thompson, *ECS Trans.* **2009**, 16, 37.
- [19] S. Kühl, A. Tarasov, S. Zander, I. Kasatkin, M. Behrens, *Chem. – Eur. J.* **2014**, 20, 3782.
- [20] A. Knop-Gericke, E. Kleimenov, M. Hävecker, R. Blume, D. Teschner, S. Zafeiratos, R. Schlögl, V. I. Bukhtiyarov, V. V. Kaichev, I. P. Prosvirin, A. I. Nizovskii, H. Bluhm, A. Barinov, P. Dudin, M. Kiskinova, X-Ray Photoelectron Spectroscopy for Investigation of Heterogeneous Catalytic Processes, in B. C. Gates, H. Knözinger, Eds., *Advances in Catalysis*, Vol. 52, Academic Press, **2009**, pp. 213 – 272.
- [21] S. Tanuma, C. J. Powell, D. R. Penn, *Surf. Interface Anal.* **1994**, 21, 165.
- [22] M. Hävecker, M. Cavalleri, R. Herbert, R. Follath, A. Knop-Gericke, C. Hess, K. Hermann, R. Schlögl, *Phys. Status Solidi B* **2009**, 246, 1459.
- [23] N. Fairley, A. Carrick, *The Casa Cookbook: Recipes for XPS data processing*, Acolyte Science, Knutsford, **2005**.
- [24] G. D. Mahan, *Many-Particle Physics*, Springer Science & Business Media, New York, USA, **2013**.
- [25] S. Doniach, M. Šunjić, *J. Phys. C: Solid State Phys.* **1970**, 3, 285.
- [26] A. Rosencwaig, G. K. Wertheim, H. J. Guggenheim, *Phys. Rev. Lett.* **1971**, 27, 479.
- [27] J. P. Perdew, K. Burke, M. Ernzerhof, *Phys. Rev. Lett.* **1996**, 77, 3865.
- [28] P. Giannozzi, S. Baroni, N. Bonini, M. Calandra, R. Car, C. Cavazzoni, D. Ceresoli, G. L. Chiarotti, M. Cococcioni, I. Dabo, A. Dal Corso, S. de Gironcoli, S. Fabris, G. Fratesi, R. Gebauer, U. Gerstmann, C. Gougoussis, A. Kokalj, M. Lazzeri, L. Martin-Samos, N. Marzari, F. Mauri, R. Mazzarello, S. Paolini, A. Pasquarello, L. Paulatto, C. Sbraccia, S. Scandolo, G. Sclauzero, A. P. Seitsonen, A. Smogunov, P. Umari, R. M. Wentzcovitch, *J. Phys.: Condens. Matter* **2009**, 21, 395502.
- [29] A. Dal Corso, *Comp. Mater. Sci.* **2014**, 95, 337 .
- [30] N. Marzari, D. Vanderbilt, A. De Vita, M. C. Payne, *Phys. Rev. Lett.* **1999**, 82, 3296.
- [31] A. A. Bolzan, C. Fong, B. J. Kennedy, C. J. Howard, *Acta Crystallogr. B* **1997**, 53, 373.

- [32] T. E. Jones, T. C. R. Rocha, A. Knop-Gericke, C. Stampfl, R. Schlögl, S. Piccinin, *Phys. Chem. Chem. Phys.* **2015**, *17*, 9288.
- [33] E. Pehlke, M. Scheffler, *Phys. Rev. Lett.* **1993**, *71*, 2338.
- [34] C. Gougoussis, M. Calandra, A. P. Seitsonen, F. Mauri, *Phys. Rev. B* **2009**, *80*, 075102.
- [35] M. Taillefumier, D. Cabaret, A.-M. Flank, F. Mauri, *Phys. Rev. B* **2002**, *66*, 195107.
- [36] A. Menzel, S. Benzaid, M. O. Krause, C. D. Caldwell, U. Hergenhausen, M. Bissen, *Phys. Rev. A* **1996**, *54*, R991.
- [37] P. J. W. Weijs, M. T. Czyżyk, J. F. van Acker, W. Speier, J. B. Goedkoop, H. van Leuken, H. J. M. Hendrix, R. A. de Groot, G. van der Laan, K. H. J. Buschow, G. Wiech, J. C. Fuggle, *Phys. Rev. B* **1990**, *41*, 11899.
- [38] V. Mauchamp, M. Jaouen, P. Schattschneider, *Phys. Rev. B* **2009**, *79*, 235106.
- [39] A. Minguzzi, O. Lugaresi, E. Achilli, C. Locatelli, A. Vertova, P. Ghigna, S. Rondinini, *Chem. Sci.* **2014**, *5*, 3591.
- [40] A. Minguzzi, C. Locatelli, O. Lugaresi, E. Achilli, G. Cappelletti, M. Scavini, M. Coduri, P. Masala, B. Sacchi, A. Vertova, P. Ghigna, S. Rondinini, *ACS Catal.* **2015**, *5*, 5104.
- [41] P. A. Zhdan, G. K. Boreskov, A. I. Boronin, W. F. Egelhoff, W. H. Weinberg, *Surf. Sci.* **1976**, *61*, 25.
- [42] J. F. van der Veen, F. J. Himpsel, D. E. Eastman, *Phys. Rev. Lett.* **1980**, *44*, 189.
- [43] S. Hüfner, G. Wertheim, J. Wernick, *Solid State Commun.* **1975**, *17*, 417 .
- [44] P. Lacovig, M. Pozzo, D. Alfè, P. Vilmercati, A. Baraldi, S. Lizzit, *Phys. Rev. Lett.* **2009**, *103*, 166101.
- [45] J. Yeh, I. Lindau, *At. Data Nucl. Data Tables* **1985**, *32*, 1.
- [46] M. Hara, K. Asami, K. Hashimoto, T. Masumoto, *Electrochim. Acta* **1983**, *28*, 1073.
- [47] A. Kotani, *J. Electron Spectrosc. Relat. Phenom.* **1996**, *78*, 7.
- [48] L. Atanasoska, R. Atanasoski, S. Trasatti, *Vacuum* **1990**, *40*, 91 .
- [49] S. W. Gaarenstroom, N. Winograd, *J. Chem. Phys.* **1977**, *67*, 3500.

- [50] N. Nücker, M. Merz, P. Schweiss, E. Pellegrin, S. Schuppler, T. Wolf, V. Chakarian, J. Freeland, Y. U. Idzerda, M. Kläser, G. Müller-Vogt, G. Er, S. Kikkawa, G. Liu, *J. Supercond.* **1999**, 12, 143.
- [51] C. T. Chen, F. Sette, Y. Ma, M. S. Hybertsen, E. B. Stechel, W. M. C. Foulkes, M. Schulter, S.-W. Cheong, A. S. Cooper, L. W. Rupp, B. Batlogg, Y. L. Soo, Z. H. Ming, A. Krol, Y. H. Kao, *Phys. Rev. Lett.* **1991**, 66, 104.
- [52] J. Augustynski, M. Koudelka, J. Sanchez, B. E. Conway, *J. Electroanal. Chem.* **1984**, 160, 233.
- [53] K. S. Kim, C. D. Sell, N. Winograd, ESCA studies of metal and metal electrode surfaces, in M. W. Breiter, Editor, *Proceedings of the Symposium on Electrocatalysis*, Physical Electrochemistry Division, Electrochemical Society, Princeton, New Jersey, **1974**, pp. 242–257.
- [54] B. Folkesson, *Acta Chem. Scand.* **1973**, 27, 287.
- [55] W.-H. Chung, C.-C. Wang, D.-S. Tsai, J.-C. Jiang, Y.-C. Cheng, L.-J. Fan, Y.-W. Yang, Y.-S. Huang, *Surf. Sci.* **2010**, 604, 118.
- [56] Y. B. Mo, I. C. Stefan, W. B. Cai, J. Dong, P. Carey, D. A. Scherson, *J. Phys. Chem. B* **2002**, 106, 3681.
- [57] A. R. Hillman, M. A. Skopek, S. J. Gurman, *Phys. Chem. Chem. Phys.* **2011**, 13, 5252.